

# We are IntechOpen, the world's leading publisher of Open Access books Built by scientists, for scientists

6,300

Open access books available

171,000

International authors and editors

190M

Downloads

Our authors are among the

154

Countries delivered to

TOP 1%

most cited scientists

12.2%

Contributors from top 500 universities



WEB OF SCIENCE™

Selection of our books indexed in the Book Citation Index  
in Web of Science™ Core Collection (BKCI)

Interested in publishing with us?  
Contact [book.department@intechopen.com](mailto:book.department@intechopen.com)

Numbers displayed above are based on latest data collected.  
For more information visit [www.intechopen.com](http://www.intechopen.com)



# Main Challenges of Heating Plasma with Waves at the Ion Cyclotron Resonance Frequency (ICRF)

*Guillaume Urbanczyk*

## Abstract

Of all the techniques used for heating plasmas in fusion devices, waves in the Ion Cyclotron Resonance Frequency (ICRF  $\sim$  MHz) continue to be exceptionally advantageous and unique insofar as it enables to deposit of power directly on ions in the core, significantly enhancing fast ion population together with fusion reaction products. However, because of the multiple inherent challenges—such as matching robustness, antenna design, wave coupling efficiency, wave propagation, wave absorption, and plasma surface interactions due to radiofrequency (RF) sheath excitation—ICRF is often one of the most complex heating systems to implement successfully. This chapter provides a brief introduction of these challenges and their respective underlying physics, together with examples of both simulations and experimental results from various tokamaks around the world. Finally, ICRF advantages and applications on present and future devices and perspectives of technological solutions are discussed and summarized.

**Keywords:** ICRF, wave coupling, RF sheath, plasma surface interactions

## 1. Introduction

The ICRF electrostatic wave is first produced by a generator called a tetrode, which is essentially a multistage amplifier of the power composed of a cascade of electron tubes. Each stage of which increases the power by approximately an order of magnitude, from watts to megawatts [1].

High-power waves enter the coaxial line of characteristic impedance  $Z_0$ , that matches the output impedance of the generator; typically,  $50\Omega$  or  $30\Omega$  as in the case of the Full-Tungsten Environment Superconducting Tokamak (WEST) [2] which **Figure 1** shows an overview of the ICRF system with all key elements.

1. Electrostatic waves then propagate towards the antenna and cross at some point the so-called *matching* unit which ensures a smooth transition between the impedance of the coaxial line  $Z_0$  and the one of the antenna straps  $Z_S$  to avoid

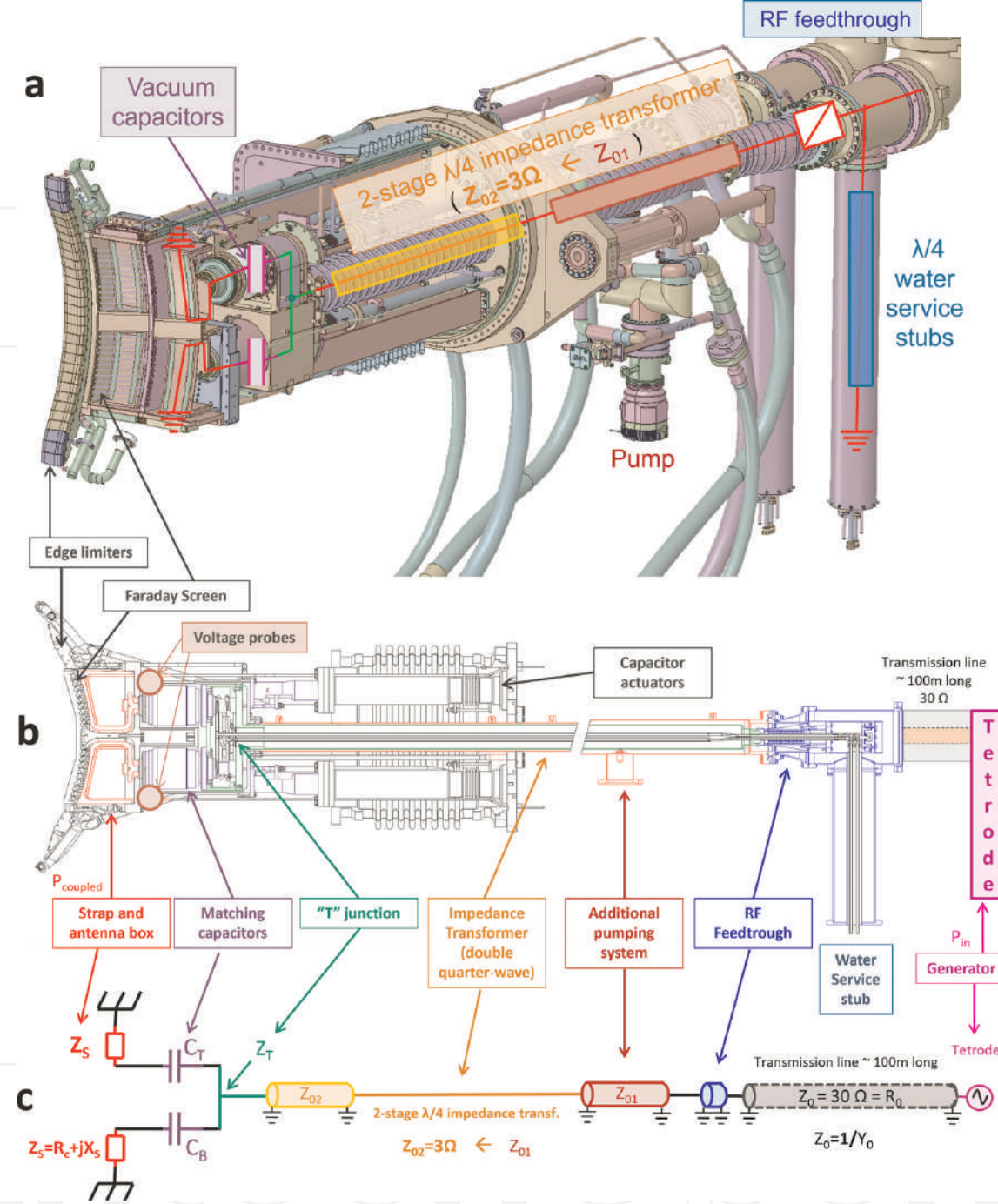


**Figure 1.** ICRF system seen in 3D (a) and from profile (b), with a schematic of the key components of the RF circuit (c) from the generator to the antenna (case of WEST tokamak) adapted from [3].

- power reflection. If successfully matched, the wave induces a current on the strap at the extremity of the transmission line.
2. This current oscillating at the ion cyclotron frequency (one the order of MHz), results in the excitation of electromagnetic ICRF waves and their *coupling* to the low-density edge plasma.
  3. These *waves* must then propagate from the edge up to the resonance layer in the core, where they can be *absorbed by the ions*. Energy is then spread to all charged particles through collisions, resulting in *plasma heating*.

These three aspects, namely the *matching*, *wave coupling*, and *absorption*, are the key points mandatory for the successful operation of an ICRF system. Section 2 provides the physics background for each of these steps, while section 3 explains what happens in practice due to all of the imperfect conditions and introduces the challenges inherent in ICRF operation; power reflection, arcing, Radiofrequency (RF) sheath excitation, erosion, impurity generation, and plasma contamination. Despite all of these challenges, the fourth and final sections present the key assets that still make ICRF an attractive auxiliary heating system and some perspectives on solutions worthy of further investigation.

## 2. The key 3 steps of ICRH (Ion Cyclotron Resonance Heating)

### 2.1 RF circuit matching

Matching the RF circuit consists of building smooth transitions between the purely real impedance of the transmission line ( $Z_0 = R_0 \approx 10 \rightarrow 50 \Omega$ ) and the complex impedance of the antenna straps ( $Z_S = R_C + jX_S$ ) which depends on the plasma. When the system is perfectly matched, the electrostatic wave flows from the generator to the straps without seeing any obstacle or being subject to any reflection. This can be achieved in many ways, relying on various components each with a variable impedance such as:

- *Single stub* also called “*trombones*” [4] in the Joint European Torus (JET) ITER-Like Antenna [5, 6] (ITER=International Tokamak Experimental Reactor), Alcator C-Mod [7] and the National Spherical Torus Experiment (NSTX) [8]
- *Double stubs loaded by shorted tunable capacitors* on TEXTOR [9] and analyzed for ASDEX-Upgrade [10]
- *Liquid stubs* arranged in a triple stub configuration in the Large Helical Device (LHD) [11] and the Experimental Advanced Superconducting Tokamak (EAST) [12]. The reactance of the short-circuited stubs of fixed geometrical length is varied by changing the height of the dielectric fluid (oil) inside the stubs
- *Fast Ferrite Tuners*: the reactance of a matching stub of fixed geometrical length is here modified by changing the magnetic characteristics of the ferrites which are disposed inside the stubs which were used in Alcator C-Mod [7] and ASDEX Upgrade [13]
- *Sliding Impedances* [14]
- *Single stubs in the Conjugate-T configuration* [15]
- *Tunable line-stretchers* (or *phase shifters*) in JET [6]
- *Tunable vacuum capacitors* in JET ITER-like antenna [16] and WEST ICRF antennas [17]. These are complex components ( $Z_C = X_L - jX_C$ ), which self-inductance ( $X_L$ ), and capacitance ( $X_C$ ) can be tuned to match any load at the strap (cf. purple elements in **Figure 1**)

If the antenna is facing vacuum, the load is stable as it basically only corresponds to ohmic losses in the antenna. In this case, almost perfect matching can be achieved with the resistive part of the load remaining small ( $R_c \approx 0.1\Omega$ ). In front of a plasma though, the load is larger than vacuum, so that  $R_c$  can increase by up to two orders of magnitude, in correlation with the efficiency by which the power is coupled.

In this case, however, the load (plasma) can change rapidly. This means  $Z_s$  is seldom if ever perfectly matched to  $Z_0$ , and that the *power* launched by the generator ( $P_{in}$ ) is hardly exactly equal to the one *coupled by the antenna to the plasma*:

$$P_{coupled} = P_{in} (1 - |\Gamma|^2) \quad (1)$$

where  $\Gamma$  is the reflection coefficient defined as  $\Gamma = (Z_s - Z_0) / (Z_s + Z_0)$ .

The fraction of uncoupled power is therefore reflected in the transmission line, which can damage the generator if it is too large. This is avoided by introducing a quarter wavelength phase-shift in the matching circuit—for instance by tuning the height of the oil in EAST stub tuner or by using an impedance transformer in WEST—so that in the section between the generator and the matching circuit, only forward waves exist.

In the section between the matching circuit and the antenna though, coexist waves travelling both forward and backward, which superimpose on one another and give rise to a standing wave pattern. The maximum and minimum voltages of such waves are defined as follows:

$$V_{max} = (1 + |\Gamma|) \sqrt{2Z_0 P_{in}} = \sqrt{2Z_0 P_{coupled} VSWR} \quad (2)$$

$$V_{min} = (1 - |\Gamma|) \sqrt{2Z_0 P_{in}} = \sqrt{2Z_0 P_{coupled} / VSWR} \quad (3)$$

And the ratio of these voltages is the so-called *Voltage Standing Wave Ratio*:

$$VSWR = \frac{1 + |\Gamma|}{1 - |\Gamma|} \quad (4)$$

It follows that VSWR grows from 1 in the ideal perfectly matched “flat-line” case ( $V_{max} = V_{min}$ ), to infinity when almost all the power is reflected. If the VSWR is too large, the difference of electrical potentials in the lines becomes so high that there is a significant risk of arcing. To prevent such deleterious events, operational safety limits are set on the voltage ( $V_{max}$ ) and the current ( $I_{max}$ ), above which the power shuts down.

$$I_{max} = (1 + |\Gamma|) \sqrt{2Y_0 P_{in}} = \sqrt{2Y_0 P_{coupled} VSWR} \quad (5)$$

with  $Y_0 = 1/Z_0$ . We now understand how crucial it is to transport the power along well-matched lines. It naturally follows that minimizing length of the lines with these undesirable effects by placing the matching system as close as possible to the antenna, will be a key aspect of the system’s efficiency (cf. section 2.5 of [18]).

In addition, *decouplers* are used to prevent the mutual coupling of adjacent lines which influence each other due to the proximity of the straps to one another. This effect can make a source behave as a receiver and endanger its generator. Decouplers are used in DIII-D [19], EAST [20], Alcator C-Mod [7], NSTX [8] and will be used on ITER [21]. This is also important to equalize the voltages at the inputs of the array and

guarantee a homogeneous excitation over the whole surface of the antenna's front face, which can otherwise have deleterious effects on local fields and RF sheath excitation. Strap-decoupling can also be improved by separating them with a septum in the antenna box to reduce mutual influence.

Excellent explanations of the topic can further be found in the fourth chapter of [18] with more detailed calculations and specific applications to the case of WEST. Once well matched, the system and the antenna are then ready to launch waves which coupling to the plasma remains to be optimized.

## 2.2 Wave coupling

The front of the antenna faces the plasma inside the vessel. As the power emitted from the generator reaches the antenna, it induces an oscillating current  $I_{RF}$  along the strap as highlighted in red in **Figures 1b** and 2, which excites ICRF waves at the edge of the plasma, as efficiently as the load or the coupling resistance ( $R_c$ ) is high.

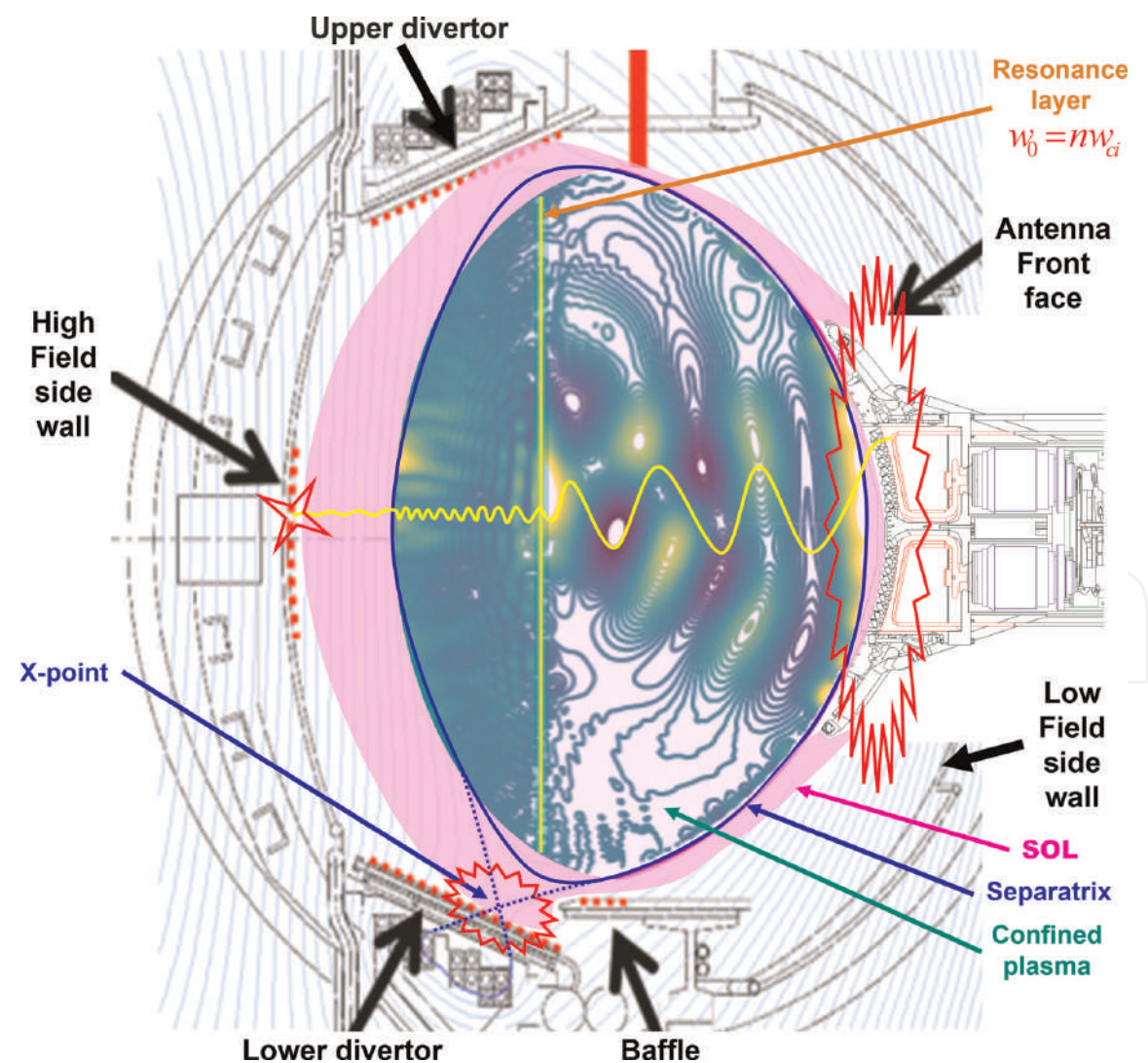


**Figure 2.**  
*Poloidal cut of a tokamak vacuum vessel, with ICRF waves excited by the antenna, propagating in the well-confined region of the plasma, partially absorbed and mode converted near the resonance layer.*

$$P_{\text{coupled}} = \frac{1}{2} R_c I_{\text{RF}}^2 \quad (6)$$

The problem in coupling ICRF waves at the edge, lies in the fact that to avoid exposure to dense and hot plasma—which would induce unacceptably large heat loads—antennas are retracted away and sit in the Scrape-Off Layer (SOL), a low-density plasma (pink regions in **Figures 2** and **3**) where the Fast Wave (FW) is generally not propagative but evanescent ( $k_{\perp}^2 < 0$ ). A wave is evanescent when the density is smaller than its cutoff density ( $n_{\text{co}}$ ). Therefore, the larger the distance from the strap to the cutoff layer ( $D_{\text{Strap-co}}$ ), the lower the coupling efficiency and vice versa. To give a rough idea, 1 cm increase of  $D_{\text{Strap-co}}$  generally results in about 20% drop of the coupling efficiency, meaning that about 1/5 of the power vanishes every centimeter until reaching densities above  $n_{\text{co}}$ . In addition, the nature of the spectrum excited by the antenna, according to its geometry (straps width, height and spacing), and in particular, the value of the parallel wave vector ( $k_{\parallel}$ ) corresponding to the main components of the spectrum, plays a key role in the coupling process:

$$R_c = \frac{Z_0}{\text{VSWR}} \sim R_0 \exp(-2 \langle k_{\parallel} \rangle D_{\text{Strap-co}}) \quad (7)$$

One can observe, in **Figure 3**, how this parameter typically influences the fast-wave cutoff density which drops by over an order of magnitude as  $k_{\parallel}$  decreases from 18 down to 6  $\text{m}^{-1}$ .

ICRF waves comport two modes called *fast* and *slow* waves in reference to their respective group velocity (details of mathematical calculations can be found in the second chapter of [22]):

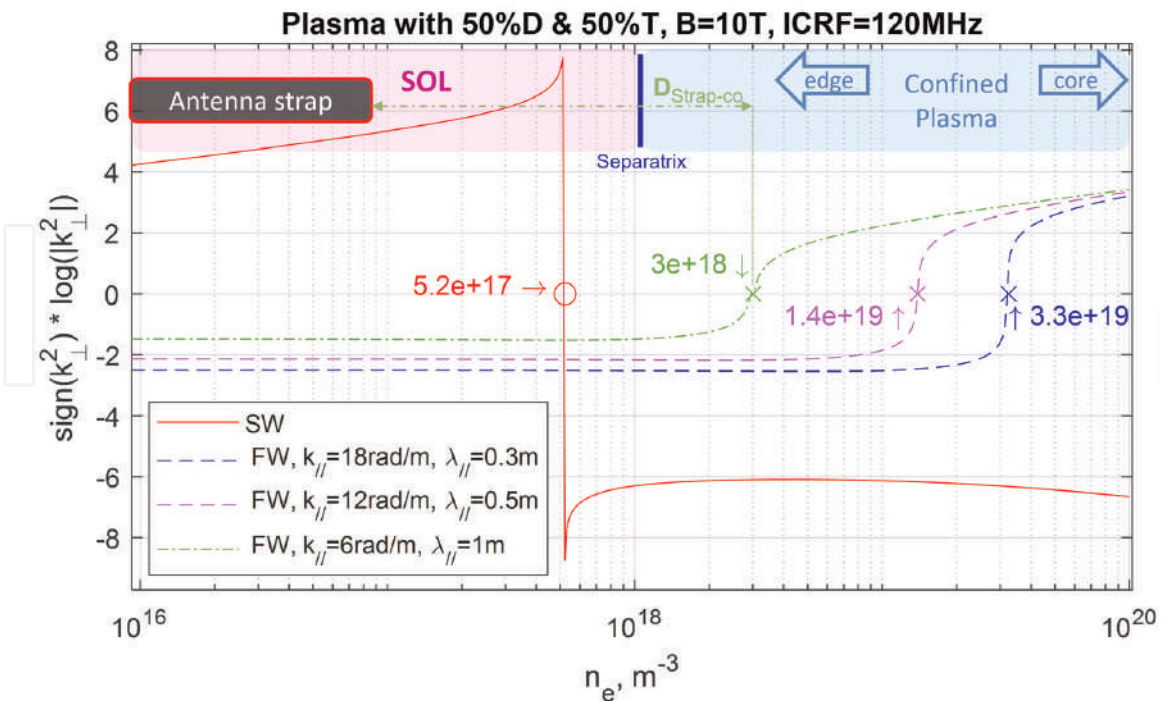


**Figure 3.** Properties of 120MHz ICRF fast (FW—dashed lines) and slow (SW—solid line) wave modes in a realistic fusion plasma with similar proportions of deuterium and tritium confined by a magnetic field of 10 tesla. Waves are propagative when the sign of  $k_{\perp}^2$  is positive, and evanescent elsewhere. Cutoff densities of each branch are written explicitly on the graph.

- *Fast Waves* (FW) are evanescent at low densities typical of the plasma edge and propagative for densities characteristic of the plasma core (**Figure 3**). FW have wavelengths on the order of few meters and an electric field perpendicular to the magnetic field. Therefore, when talking about coupling maximization, it is common to implicitly refer to this mode, because it is the one suited to heating the ions which rotate perpendicularly around the magnetic field lines.
- *Slow Waves* (SW) are propagative at very low densities characteristic of the outer most “far” SOL ( $n_e < 5.2 \cdot 10^{17} \text{ m}^{-3}$  in **Figure 3**) and evanescent above. SW have millimetric wavelengths and an electric field parallel to the magnetic field. Because the current straps are not perfectly perpendicular to the tilted magnetic field lines, SW are parasitically excited and are often responsible for exciting the RF-sheath, leading to deleterious plasma surface interactions. The role the faraday screen (**Figure 1a**) with bars in principle parallel to the magnetic field, is intended to locally increase the conductivity in the parallel direction to screen the SW in front of the straps. Unfortunately, we will see in the next section that this is not enough.

At this point, one should remember when hearing people say that they are trying to “optimize the coupling of an ICRF antenna”, that they are basically trying to maximize its coupling resistance ( $R_c$ ), either by reducing  $D_{\text{Strap-co}}$  or  $k_{//}$  (Eq. (7)).

$D_{\text{Strap-co}}$  can be minimized in different ways [23]:

- Put the *antenna closer to the plasma*, but this will come with stronger heat loads and usually impurity production
- *Globally increase the density* of the plasma, but this is limited and associated with an increase of the power lost in radiations
- *Locally increase the density* by fueling the plasma from valves magnetically connected to the antenna and ideally as close as possible to the middle plane [24, 25]
- *Increase the frequency* of the waves, which must remain compatible with an efficient scenario for heating the plasma (discussed in the next section)

$k_{//}$  can be minimized at two different stages:

- While designing the antenna, basically by increasing the space between adjacent straps, but this often limited by the available space in the torus
- During the experiments, by reducing the phase difference of the currents on the adjacent straps ( $\phi$ ). Most of the time however, this trick is first limited by the currents induced on the surrounding passive structures, which play an important role in plasma surface interactions [26]. These currents basically tend to add up when currents are in phase (monopole  $\phi=0^\circ$ ) instead of compensating each other for largest phasing (dipole  $\phi=180^\circ$ ) [27]. Secondly, the larger  $k_{//}$  the more efficient the wave absorption [28].

Once efficiently coupled to the plasma, wave absorption remains to be optimized.

## 2.3 Wave absorption

Waves that propagate towards the center of the plasma finally reach the resonance layer where ions frequency ( $\omega_0$ ) corresponds to a multiple of the wave frequency ( $n\omega_{ci}$ ), enlightened by the vertical yellow line in **Figure 2**. In this region, the frequency of the wave coincides with the fundamental or harmonics of the cyclotron frequency of ion species to be heated. One can tune the wave frequency, the magnetic field profile, and the plasma composition to pick the desired heating scheme among a variety of techniques [29] by matching the Doppler-shifted wave frequency with the ion cyclotron harmonics:

$$\omega = n\omega_{ci} + k_{\parallel}v_{\parallel,i} \quad (8)$$

- *Heating a minority at its fundamental resonance* ( $n=0$ ): such as hydrogen in a deuterium plasma (H-D) with a small concentration of hydrogen, typically  $n_H/n_H+n_D < 15\%$ . So far, minority heating is the most routinely used in most devices. However, while it has long been applied on two-ion species plasmas, it has been found that it can also be applied with great efficiency in plasmas with three (or more) ion species.
- The *three-ions scheme* also consists in heating the fundamental of the minority specie such as a little helium in a deuterium tritium fusion plasma (ex:  $(\text{He}^3)\text{-DT}$ ), but here the resonance location of the minority must fall in between the resonances of both others majority species [30], where the amplitude of the left-handed polarization ( $E_+$ ) can reach very high values and lead to strong diffusion (D) of the wave power:

$$D \propto |J_0|^2 |E_+|^2 \quad (9)$$

- *Heating a majority at its harmonic resonance* ( $n>0$ ): this can be an alternative to the minority heating typically if it proves challenging to accurately controlling the isotopic ratio. However, this scenario becomes truly effective only when a population of fast ions is created to improve power absorption. This process usually relies on harmonic heating. While generating a population of fast ions large enough to boost up the absorption, it can also be directly injected by a Neutral Beam Injector (NBI), hence the so-called synergy between NBI and ICRH (cf. experimental [31] and simulation [32] results in JET tokamak). Unfortunately, not only NBI is not available in all devices, but if the confinement is not good enough, for instance in case of low plasma current, this method is counteracted by fast-ions losses.

## 3. Challenges behind each step

### 3.1 Real-time matching

In practice, before main experiments start, ICRF operators usually “prepare the matching” and pre-set the parameters (ex: Oil level in the stub tuner in EAST, capacitance of the capacitors in WEST ...) with the antenna facing vacuum. Later, the matching is adjusted with the antenna facing the plasma, one of the many reasons why

campaigns always include a period for commissioning systems at the beginning. The system starts with low power in case of sources of mismatch or poor coupling efficiency to avoid the risk of arcing due to large fractions of power reflected, and gradually raise it up to power levels relevant for the experiments (MW order). One of the key goals during the experiments is to further improve plasma confinement, often leading to operate in H-mode [33]. H-mode plasmas represent a great challenge for all RF circuit matching, first because during the L-H transition, a pedestal forms at the edge where the density typically drops with sharper gradient compared to L-mode plasmas, lowering the coupling efficiency ( $R_c$ ) sometimes by half. But also, the so-called Edge-Localized Modes (ELMs) induce important load variations through transient bursts, basically as large as their frequency is low (from kHz range for the smallest type-III ELMs down to tens of Hz for the largest type-I ELMs with  $R_c$  suddenly increasing by factors up to 5 within less than a millisecond. One can further show for a strap matched by a 2-port matching unit, if the matching is not reconfigured, the VSWR will raise in similar proportions as  $R_c$  (cf. calculation details in section 2.7 of [18]), risking provoking arcs either in the transmission lines [34] or in the antenna box [35]. All this motivates real-time control of the impedance matching that can be achieved with:

- *Capacitors*, like in Tore Supra Classical antennas [36] and JET-ILA [37]. Amplitudes of the incident and reflected voltages and their phase shift are typically measured either on the transmission lines or ideally as close as possible to the antenna, and mixed to provide error signals driving the capacitors
- *Conjugate-T* and similar principle as with capacitors [13]
- *Fast Ferrite Tuners*, like in Alcator C-mod antennas [7]
- Impedance matching by real-time controlling the *generator's frequency* [4]
- *Decouplers* and *double stub* in ITER [21]

Various algorithms can then be used to automatically tune parameters of interest for each component. However so far, no controller allows tackling sub millisecond variations typically induced by ELMs, hence the need for so-called *load resilient* matching schemes [38].

### 3.2 Load resilience

Without load resilience, an ICRF system would stop delivering power every time its VSWR would exceed some safety value, which would basically make it incompatible with steady operation during a discharge with ELMs. A very convincing comparison between resilient and non-resilient system can be found in Figure 13 of [13].

Among existing load-resilient schemes, one can quote:

- *3dB hybrid coupler* diverting the reflected power to a dummy load, such as the lossy network in ASDEX-Upgrade [39]
- *Conjugate-T* concept, connecting pairs of straps, with various designs:

- *External* conjugate-T relying on line-stretchers in JET [13] and EAST [40]
- *Internal* conjugate-T relying on capacitors in JET-ILA [5], Tore Supra [41] and WEST [17]
- *Stub* conjugate-T in Alcator C-Mod [15]

More details can be found on the conjugate-T under section 4 of the fourth chapter of [18] with detailed mathematical calculations and applications to the internal conjugate-T of WEST and experimental results in [42].

- *Travelling wave antenna* concept [43] which in case of load drop, takes profit from the mutual coupling between straps to let the wave propagate along the array and recirculate, making it inherently load resilient. This concept has been used in DIII-D [44, 45] for driving current and envisaged for heating plasmas in WEST [46]. While never tested for heating tokamak plasmas, the concept somehow lost its appeal, essentially due to the integration challenges it raises, that become even more problematic in the perspective of fusion reactors which must maximize the surface of the tritium breeding blanket and therefore focus on heating systems with large power densities.

Note that in most of the cases, load resilient solutions are combined with matching units, so that the problem is most often tackled from the generator perspective, with first goal to deliver constant power despite load fluctuations at the antenna.

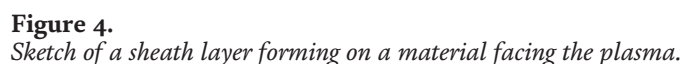
After having explained the importance of operating with a well-matched system, we will now place ourselves from the inner vessel perspective and further discuss the challenges that concern an ICRF antenna facing a fluctuating plasma. There the main goal will rather be to prevent the coupling resistance from dropping under some value, not only critical for the VSWR and arcing in the transmission lines, but also for the excitation of near fields and RF sheath.

### 3.3 RF-sheath and potential rectification

The formation of a sheath on any component facing the plasma is a natural phenomenon [47]. The sheath is a thin layer (usually few millimeters wide) which forms on the surface of all materials in contact with the plasma. Across this layer, a separation of the charges (therefore an electric field) makes it possible to preserve the ambipolarity of the fluxes of charged particles from the plasma towards a surface (cf. **Figure 4**). Since the mass of electrons is much smaller than that of ions, their speed is much greater. Therefore, when exposed to a plasma, the surface of materials becomes negatively charged, repelling electrons, and attracting ions approaching below a *Debye length* ( $\lambda_{De} = \sqrt{\epsilon_0 k_B T_e / n_e e^2}$ ) with  $\epsilon_0$  and  $k_B$  respectively electric and Boltzmann constants,  $T_e$  and  $n_e$  respectively the electron temperature and density and the charge of the electron  $e = 1.6 \times 10^{-19}$  coulombs.

The properties of the sheath can undergo substantial changes depending on several parameters that can typically influence its electric field and width  $\delta_{sheath}$ :

$$\delta_{sheath} = \lambda_{De} \left( \frac{e \cdot V_{DC}}{k_B T_e} \right)^m \quad (10)$$



with  $V_{DC}$  the DC potential and  $m$  a parameter that typically changes between  $2/3$  and  $3/4$  depending on the incidence angle of magnetic field lines on materials and the collisional properties of the sheath as explored through Particle in Cell simulations in [48]. In general, the electric field accelerates the ions towards the wall, leading to an increase of the sputtering and the production of impurities (**Figure 4**) in proportions usually comparable to the increase in electron temperature:

On the other hand, in the presence of ICRF heating, this phenomenon is further aggravated by the so-called *rectification* of the oscillating potentials associated with the *slow wave* carrying electric field in the direction parallel to the magnetic field lines (cf. red curve in **Figure 3**). Let us now express the *current instantly conducted to any object exposed to the plasma* as:

with  $I_{\text{sat}}^+$  the ion saturated current,  $\phi_f$  the floating potential and  $\tilde{V}(t) = V_{DC} + V_{RF} \cos(\omega_0 t)$  the sheath potential in presence of an RF wave. Then the RF  $\rightarrow$  DC rectification, specific to waves at the ion cyclotron frequency, results from the fact that the electrons (light compared to the ions) react instantaneously to the oscillating electric field of the wave ( $V_{RF}$ ), while the ions react only to the *average value*.

11

with  $I_0$  a Bessel function. The consequence at the level of the components facing the plasma on the scale of an RF period, is the appearance of a DC current due to the privileged drift of the electrons. Thus, to compensate this current, the DC potential of the sheath must adjust and get biased by an extra potential  $V_b$ :

$$V_b = \frac{k_B T_e}{e} I_0 \left( \frac{e V_{RF}}{k_B T_e} \right) \quad (14)$$

The RF  $\rightarrow$  DC rectification of the sheath therefore has the effect of increasing the potential drop (electric field) through the skin between the plasma and the wall, i.e., the acceleration of the ions towards the materials. This acceleration often boosts ions incident energies up to critical levels for exposed components (i.e., above sputtering yields threshold values). For deeper understanding of the topic, the reader is highly encouraged to refer to excellent tutorial [49] and reviews of key experimental [26–50] and modelling [51] results.

### 3.4 Physical sputtering yield

The other key process by which ICRF operation often enhances impurity production is the physical sputtering yield  $Y_{\text{Eff}}$ . This parameter represents the probability for an ion to sputter an atom from a target, given its charge, its incident energy, and their respective mass:

$$\text{Impurity outflux} = \Gamma_{\text{target atoms out}} = \Gamma_{\text{ion in}} Y_{\text{Eff}} \quad (15)$$

For example, the graph in **Figure 5** shows how the sputtering of a graphite ( $\sim$ carbon) target evolves for different bombarding species. The first important aspect of the sputtering yield is that it varies non-linearly with the energy of the incident ion. The second one is that only above a threshold energy of about 30eV, do the incident species start to sputter carbon atoms. The red curve also represents the self-sputtering of lithium which is sometimes used for material coating to prevent from important plasma contamination by high-Z impurities. One can see that a lithium coating will typically get eroded at much lower energy, while plasma facing components in graphite will require larger energies. We have here taken the case of carbon components, sometimes coated with lithium, exposed to various species, which is the case in EAST tokamak. Carbon however won't be used in future devices plasma facing components due to tritium retention. Tungsten has now become the most suitable candidate. In WEST for instance, antenna limiters are coated with tungsten, which sputtering follows similar trends (cf. **Figure 3** of [23]).

### 3.5 Poor coupling efficiency and near-field effects

RF-sheath excitation is the phenomenon proper to ICRF which is responsible for its peculiar complexity, due to the non-linear trade-off relation between the maximization of the coupling and the minimization of the interactions with the plasma. For any object in principle, moving away from the plasma results in a strict decrease of their interactions. However, for a classic ICRF antenna, moving away first induces a drop in its coupling efficiency, therefore an increase of excited fields (consistent with an increase of the VSWR in the transmission lines), which in turn can in critical cases result in a local but exponential increase of the RF sheath potential (cf. **Figure 3** of [52]).

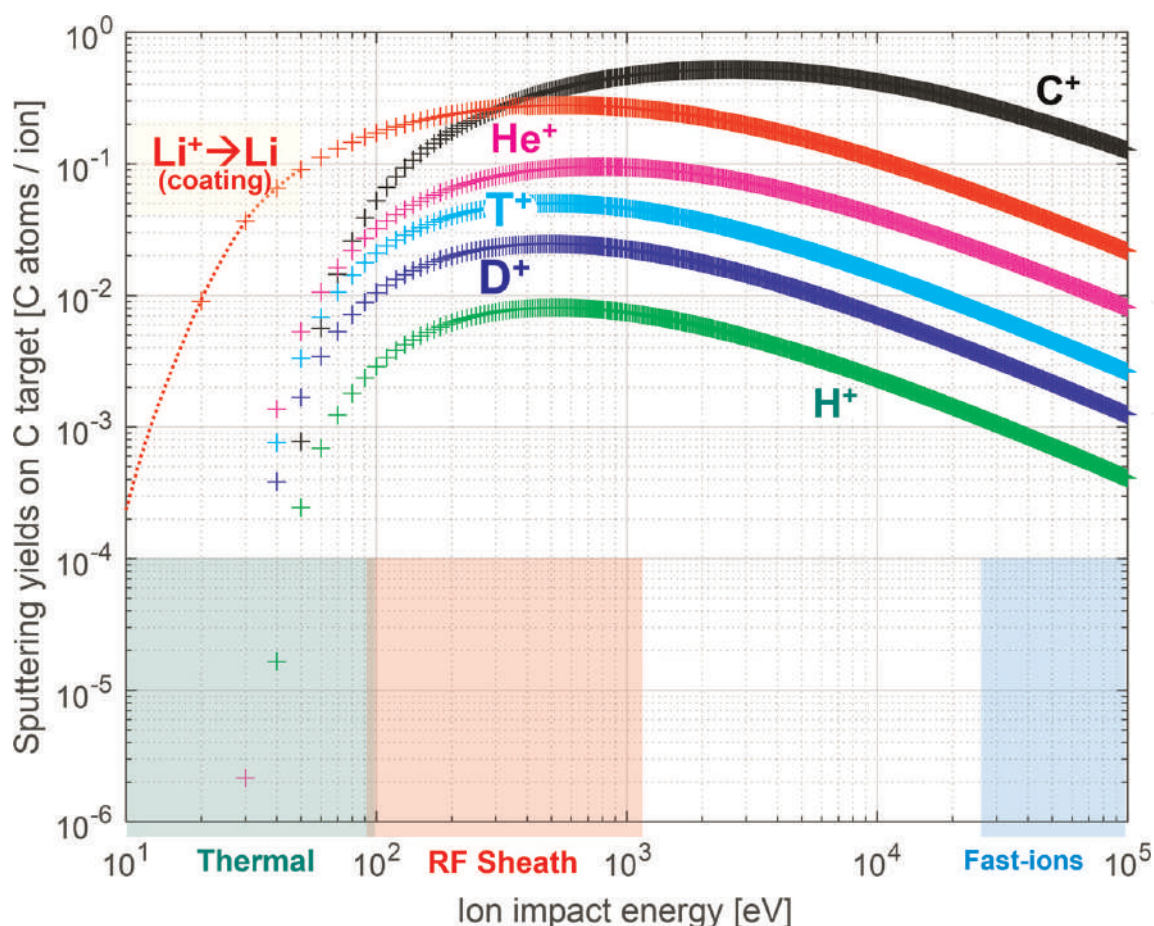


**Figure 5.**  
 Sputtering yield of various ion species on a target in graphite.

and section 3.3 of this chapter). In addition, the sputtering yield not only changes non-linearly, but also reaches its largest values for energies typically in the range of potential rectified by RF sheaths (cf. red region between 100eV and 1keV in **Figure 4**). It follows that in some cases, increasing the distance between an ICRF antenna and the plasma to reduce their interactions based on linear intuition, can unexpectedly cause an increase of impurity production from local sources, reacting to sharp increase of RF sheath potentials. These phenomena can be modeled in different ways as summarized in [53]. This behavior was also experimentally observed in WEST during a scan of the radial position of an ICRF antenna, where the floating potential measured by a reciprocating probe did not directly decrease as the antenna was retracted but first passed by a maximum for intermediate position (cf. Figure 4 in [50] or Figure 6.23 of [22] in open access). A wide variety of RF-sheath induced plasma surface interactions have also been observed in devices such as:

- EAST with the partial melting of metallic plates at the corners of an ICRF antenna, which precisely did not melt at the closest point to the plasma, but at the locations where simulations predict RF sheath excitation to be maximal (cf. Figure 14 in [54] or Figure 6.27 of [22] in open access)
- Tore Supra with large, enhanced potentials measured with retarded field analyzer [55] causing large heat loads on antennas [56]

- A LineAr Plasma Device (LAPD) using diagnostic magnetically connected to ICRF antenna along large number of reproducible discharges to provide great evidence of ICRF interaction process in the edge plasma [57]
- Alcator C-Mod with strong potentials measured with several different probes [58] caused by RF sheath excitation [59], leading to the increase of impurity sources and deleterious influence on plasma performance [60]
- ASDEX Upgrade with similar experiments [61] that have inspired a series of successful technological upgrades [62, 63] discussed hereafter in section 4
- JET is also subject to these effects [26, 64]

Interactions occurring at vicinity or in regions magnetically connected to the active antenna frame (red star with most branches around the antenna in **Figure 2**) are often classified as *near field effects*. Hence, interactions respectively taking place elsewhere will be conveniently referred to as *far field effects*<sup>1</sup>.

### 3.6 Abnormal wave absorption and far-field effects

Following the same logic, we will categorize interactions occurring in regions without magnetic connection to the active antenna as *far field effects*. These can be observed in unexpected locations when abnormal propagation and absorption of the wave take place. For instance, if the absorption efficiency is low, the power launched in the plasma is not fully absorbed at the first pass, and a non-negligible fraction of unabsorbed power propagates and reflects on farther objects such as the divertor or the inner wall as represented in **Figure 2**. In these cases, not only heating performance drop, but RF-sheath can also potentially become excited in global fashion. Such effects were well-observed in

- EAST *high field side wall* (cf. red star with 4 branches in **Figure 2**) when the antenna operated in monopole phasing, causing a drop in the absorption efficiency and an increase of fields excitation at the inner wall [54]
- WEST *divertor* if too low hydrogen ratio leads to poor wave absorption [65]
- NSTX *divertor* where operating at high harmonics led to the excitation of surface waves [66] and substantial fraction of their power to be coupled to the edge filamentary structures parallel to the magnetic field lines [67], resulting in potential rectification at their extremity and deleterious interactions [68].

---

<sup>1</sup> Here, *near* and *far field effects* should not be confused with the near and far electromagnetic fields diffusion patterns around an object, but simply refer to the location where the effect occurs with respect to the ICRF antenna.

## 4. The beauty of ICRH: assets and technological perspectives

### 4.1 Assets

Despite the many challenges, ICRF has remained a very important tool for heating plasmas, with constant progress over the past fifty years [69]. ICRF is the only heating system that can directly deposit power onto the ions, allowing to generate fast ions and significantly boost fusion performance. While minority heating has long remained the most widely used method, this past two decades have been marked by the emergence of several modelling tools allowing to predict wave absorption efficiency [70] and power thermalization on the various species [71, 72]. These tools have allowed to explore much wider varieties of heating schemes [29]. Most promising ones were then tried experimentally, and their efficiency confirmed. One can typically quote scenarios based on the synergy with NBI [31, 32, 73] and these relying on three-ion scheme [74]. In particular, the three-ion scheme has gained increasing interest not only due to the efficiency in generating fast ions, but also for the operation flexibility it offers. Indeed, instead of relying on specific fraction of a minority specie—which can be difficult to maintain over operation—it proves much easier to keep control of rough proportions of two (or more) majority species and deposit power on a third very minor one which fraction is easier to control. Most promising scenario for fusion reactor D-T plasmas would therefore consist in depositing power most likely on  $^3\text{He}$ , which has been successfully achieved in JET and Alcator C-Mod [30] and foreseen for future devices like ITER [74] and SPARC [75].

Another application of ICRH is the control of impurity population in the core. It has for instance been observed in JET, that for ICRF power above 4MW, heating H minority can result in high-Z impurity screening out of the core [76]. Furthermore, the three-ion scheme even allows to directly pump out an impurity by depositing part of the power on it. This was observed with beryllium in JET [29], with Argon on TFR [77] and Alcator C-Mod [78]. The same trick could further allow to pump out tungsten impurity by targeting the second harmonic of  $\text{W}^{56+}$  in SPARC's high temperature plasmas [78], a powerful tool to prevent tungsten accumulation in the core.

### 4.2 Technological perspectives

A few research and development ideas for improving current design of antennas yet remain to be tested. One can quote:

- *Travelling wave antennas* [43] could improve the reliability of ICRF systems thanks to its inherent load resilience and much larger coupling capacities, offering the possibility to place the antenna 10cm further away from the plasma than a classic antenna and still be able to couple similar amount of power. This could have tremendous impact not only on the coupling efficiency but also on the interactions with the plasma and its contamination by metallic impurity. The disadvantage of this concept is its low power density due to the large number of straps ( $>5$ ). This makes any design hardly compatible with fusion reactor worried of maximizing the surface of the tritium breeding blanket. But maybe some tricks have not yet been thought about ...

- *Active limiters* could allow compensating actively the image currents induced on limiters by nearby current straps. Relying on the concept of proximity effect [27], these currents can be cancelled by powering straps with appropriate phasing and power ratio, as was shown in ASDEX-Upgrade 3-strap antennas [63] and Alcator C-Mod 4-strap antennas [79]. However, operating the ICRF system with optimal settings is not only challenging in terms of control, but mostly limiting in terms of power density. *Active limiters* would then consist in applying a fraction of the power sent on the straps, directly on the limiters. This could allow reducing the local impurity sources, by canceling off the local currents that tend to be responsible for RF sheath excitation. In addition, such solution would offer two key advantages:
  - *more flexibility* during ICRF operation by opening the possibility to routinely tune the antenna *phasing* without aggravating interactions with the plasma. In other words, this would allow operating with different antenna spectra to cope with plasma changes regardless of near-field effects

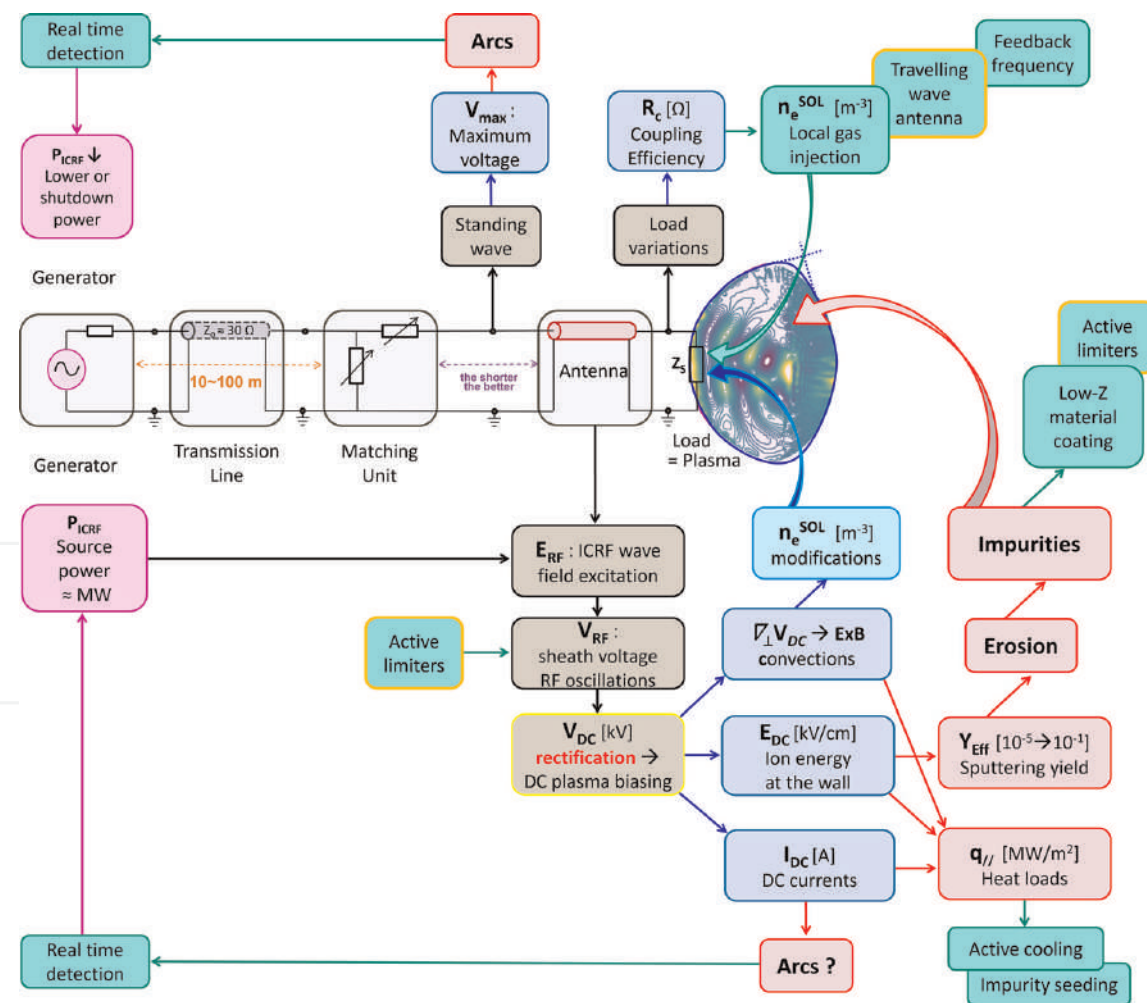


**Figure 6.** Summary of the key components of an ICRF system, and a selection of the main phenomena that can occur in various location. Black boxes enlighten phenomena inherent to ICRF powering. Blue boxes show the physical parameters that are most directly influenced. Red boxes show the potentially deleterious consequences of parameters changes. Green boxes with green and orange borders show the main solutions respectively existing and to be explored.

- *maximize power density*. While this is already quite important in nowadays experimental tokamaks, it will be a critical aspect on future fusion reactors, which aim at maximizing the surface of the tritium breeding blanket for producing fuel and extracting the energy radiated by the plasma to generate electricity. Simultaneously satisfying requirements on plasma heating, fuel production and energy exhaust, pushes towards more compact designs with larger power density currently hardly compatible with low level of impurity production. Active limiters could therefore be a major technological solution.

## 5. Conclusion

Despite all challenges, heating fusion plasmas with waves in the ion cyclotron range of frequency is still very attractive. While several technological solutions remain to be explored, a variety of existing ones are already routinely used and allow successful operation in many devices around the globe. A summary of the key components of an ICRF system, and a selection of the main phenomena that can occur in various location is provided in **Figure 6**. To conclude on the perspective of fusion reactors, while ICRF may not be the optimal solution in terms of power density, note that as the intensity of the magnetic field due to progress made on low temperature superconductors and the size of the devices will increase, ICRF is the only heating system which difficulty to implement will not be affected.

For further reading of on this topic, the reader is highly encourage to refer to a review of the “Recent Progress in ICRF in Magnetic Confinement Fusion” [80] and references therein.

## Acknowledgements

Laurent Colas, Julien Hillairet, Karl Vulliez, Annika Ekedahl, and more globally WEST and EAST ICRF Teams are warmly acknowledged for their efforts in making experiments possible and the numerous fruitful discussions. I also want to thank a lot Wouter Tierens, Mari Usoltceva, Vladimir Bobkov, and the rest of ASDEX ICRF team, Ernesto Lerche from ERM and colleagues from the 107 team of Institut Jean Lamour for all the things we collaborated over the past few years.

## Author details

Guillaume Urbanczyk  
Institute of Plasma Physics, Chinese Academy of Sciences, Hefei, China

\*Address all correspondence to: [guiguiurban@hotmail.com](mailto:guiguiurban@hotmail.com)

## IntechOpen

© 2022 The Author(s). Licensee IntechOpen. This chapter is distributed under the terms of the Creative Commons Attribution License (<http://creativecommons.org/licenses/by/3.0>), which permits unrestricted use, distribution, and reproduction in any medium, provided the original work is properly cited. 

## References

- [1] Faugel H, Bobkov V, Fünfgelder H. The prospects of ICRF generators at ASDEX upgrade. AIP Conference Proceedings. 2020;**2254**:070006. DOI: 10.1063/5.0013529
- [2] Bourdelle C et al. WEST Physics Basis. Nuclear Fusion. 2015;**55**:063017. DOI: 10.1088/0029-5515/55/6/063017
- [3] Vulliez K, Chen Z, Ferlay F, Winkler K, Helou W, Hillairet J. The mechanical structure of the WEST ion cyclotron resonant heating launchers. Fusion Engineering and Design. 2015; **96–97**:611-615. DOI: 10.1016/j.fusengdes.2015.06.050
- [4] Wade TJ, Jacquinot J, Bosia G, Sibley A, Schmid M, et al. Development of the JET ICRH plant. Fusion Engineering and Design. 1994;**24**:23-46. DOI: 10.1016/0920-3796(94)90035-3
- [5] Durodié F, Dumortier P, Blackman T, Wooldridge E, Lerche E, Helou W, et al. ITER-like antenna for JET first results of the advanced matching control algorithms. Fusion Engineering and Design. 2017;**123**(November):253-258. DOI: 10.1016/j.fusengdes.2017.05.113
- [6] Monakhov I, Graham M, Blackman T, Dowson S, Durodie F, Jacquet P, et al. Design and operations of a load-tolerant external conjugate-T matching system for the A2 ICRH antennas at JET. Nuclear Fusion. 2013;**53**(8):083013. DOI: 10.1088/0029-5515/53/8/083013
- [7] Lin Y et al. ICRF antenna matching systems with ferrite tuners for the Alcator C-Mod tokamak. Fusion Engineering and Design. 2015;**100**: 239-248. DOI: 10.1016/j.fusengdes.2015.06.022
- [8] Swain DW et al. Loading and asymmetry measurements and modeling for the national spherical torus experiment ion cyclotron range of frequencies system. Fusion Science and Technology. 2003;**43**:503-513. DOI: 10.13182/FST03-A297
- [9] Durodié F, Vervier M. First results of the automatic matching device for textor's ICRH system, Fusion Technology. 1992. pp. 477-480. DOI: 10.1016/B978-0-444-89995-8.50088-6. ISBN 9780444899958
- [10] Hangan D-M et al. Analysis of dynamic matching networks for the ICRF system at ASDEX upgrade. Fusion Engineering and Design. 2011;**86**: 736-741. DOI: 10.1016/j.fusengdes.2011.02.001
- [11] Saito K et al. Real-time impedance matching system for ICRF heating in LHD. Fusion Engineering and Design. 2008;**83**:245-248. DOI: 10.1016/j.fusengdes.2008.01.017
- [12] Zhao Y-P et al. EAST ion cyclotron resonance heating system for long pulse operation. Fusion Engineering and Design. 2014;**89**:2642-2646. DOI: 10.1016/j.fusengdes.2014.06.017
- [13] Braun F et al. ICRF system enhancements at ASDEX upgrade. Fusion Engineering and Design. 2001; **56–57**:551-555. DOI: 10.1016/S0920-3796(01)00274-5
- [14] Lamalle PU et al. Commissioning of the wideband matching system for ICRH of ELMy JET Plasmas. AIP Conference Proceedings. 2001;**595**:118
- [15] Parisot A. Design of an ICRF fast matching system for the Alcator C-Mod tokamak. PhD Thesis. 2004. Available from: <https://dspace.mit.edu/bitstream/handle/1721.1/93763/>

04RR002\_full.pdf?sequence=1&isAllowed=y

[16] Durodié F et al. Physics and engineering results obtained with the ion cyclotron range of frequencies ITER-like antenna on JET. *Plasma Physics and Controlled Fusion*. 2012;**54**:074012. DOI: 10.1088/0741-3335/54/7/074012

[17] Helou W, Colas L, Hillairet J, Milanesio D, Mollard P, Argouarch A, et al. Radio-frequency electrical design of the WEST long pulse and load-resilient ICRH launchers. *Fusion Engineering and Design*. 2015;**96–97** (October):473-476. DOI: 10.1016/j.fusengdes.2015.01.005

[18] Helou W. Design and operation of antennas at the ion cyclotron and lower hybrid range of frequencies for nuclear fusion reactors. PhD Thesis. 2017. Available from: <http://www.theses.fr/2017AIXM0395>

[19] Goulding RH, Hoffman DJ, Ryan PM. Power compensators for phased operation of antenna arrays on JET and DIII-D. *AIP Conference Proceedings*. 1994;**289**:351. DOI: 10.1063/1.44958

[20] Gen C, Mao YZ, Zhao YP, Yuan S, Zhang XJ, Qing CM. Development and test of decoupler for ICRF antenna in EAST. *Fusion Engineering and Design*. 2016;**107**:32-37. DOI: 10.1016/j.fusengdes.2016.04.010

[21] Grine D et al. Summary and results of the study of the hybrid matching option implementation of the ITER ICRH system. *Fusion Engineering and Design*. 2012;**87**:167-178. DOI: 10.1016/j.fusengdes.2011.12.006

[22] Urbanczyk G. Interaction of High-Power waves with the plasma periphery of WEST & EAST tokamaks. PhD

Thesis. 2019. Available from: <https://hal.univ-lorraine.fr/tel-02517768/document>

[23] Urbanczyk G, Colas L, Hillairet J, Lerche E, Fedorczak N, et al. RF wave coupling, plasma heating and characterization of induced plasma-material interactions in WEST L-mode discharges. *Nuclear Fusion*. 2021;**61**:086027. DOI: 10.1088/1741-4326/ac0d11

[24] Urbanczyk G, Zhang XZ, Colas L, et al. Optimization of discharges with ion cyclotron range of frequencies using local gas injection in EAST. *Nuclear Fusion*. 2019;**59**:066023. DOI: 10.1088/1741-4326/ab1610

[25] Zhang W, Jacquet P, Lerche E, Bilato R, Bobkov V, et al. 3D simulations of gas puff effects on edge plasma and ICRF coupling in JET. *Nuclear Fusion*. 2017;**57**:056042. DOI: 10.1088/1741-4326/aa6817

[26] Bobkov V, Aguiam D, Bilato R, Brezinsek S, Colas L, et al. Impact of ICRF on the scrape-off layer and on plasma wall interactions: From present experiments to fusion reactor. *Nuclear Materials and Energy*. 2019;**18**:131-140. DOI: 10.1016/j.nme.2018.11.017

[27] Colas L, Lu L-F, Křivská A, et al. Spatial proximity effects on the excitation of Sheath RF voltages by evanescent slow waves in the ion cyclotron range of frequencies. *Plasma Physics and Controlled Fusion*. 2017;**59**:025014. DOI: 10.1088/1361-6587/59/2/025014

[28] Lerche E, Bobkov V, Jacquet P, Mayoral M-L, Messiaen A, et al. Recent experiments on alternative dipole phasing with the JET A2 ICRF antennas. *AIP Conference Proceedings*. 2009;**1187**:93. DOI: 10.1063/1.3273845

- [29] Lerche E, Van Eester D, Jacquet P, Casson F, et al. ICRH options for JET-ILW DTE2 operation. AIP Conference Proceedings. 2020;**2254**:030007. DOI: 10.1063/5.0013530
- [30] Kazakov Y, Ongena J, Wright J, et al. Efficient generation of energetic ions in multi-ion plasmas by radio-frequency heating. Nature Physics. 2017;**13**: 973-978. DOI: 10.1038/nphys4167
- [31] Kirov KK, Kazakov Y, Nocente M, Ongena J, et al. Synergistic ICRH and NBI heating for fast ion generation and maximising fusion rate in mixed plasmas at JET. AIP Conference Proceedings. 2020;**2254**:030011. DOI: 10.1063/5.0014235
- [32] Huynh P, Lerche EA, Van Eester D, Bilato R, et al. Modeling ICRH and ICRH-NBI synergy in high power JET scenarios using European transport simulator (ETS). AIP Conference Proceedings. 2020;**2254**:060003. DOI: 10.1063/5.0014240
- [33] Keilhacker M et al. Confinement studies in L and H-type Asdex discharges. Plasma Physics and Controlled Fusion. 1984;**26**(1A):49-63. DOI: 10.1088/0741-3335/26/1A/305
- [34] Bobkov V. Studies of high voltage breakdown phenomena on ICRF antennas. 2003. Available from: <http://mediatum.ub.tum.de/doc/602957/document.pdf>
- [35] Bobkov V, Braun F, Hartmann DA, et al. Influence of ELMs on operation of ICRF antennas in ASDEX Upgrade. Journal of Nuclear Materials. 2005; **337–339**:776-780. DOI: 10.1016/j.jnucmat.2004.10.109
- [36] Ladurelle L, Agarici G, Beaumont B, et al. First results of automatic matching system on Tore Supra ICRH antennas: fast matching network for ICRH systems. In: Proceedings of 19th SOFT. Lisbonne, Portugal; 1996. DOI: 10.1016/B978-0-444-82762-3.50118-X
- [37] Durodié F, Dumortier P, Helou W, et al. Circuit model of the ITER-like antenna for JET and simulation of its control algorithms. AIP Conference Proceedings. 2015;**1689**(070013). DOI: 10.1063/1.4936520
- [38] Noterdaeme J-M, Bobkov V, Brémond S, Parisot A, et al. Matching to ELMy plasmas in the ICRF domain. Fusion Engineering and Design. 2005;**74**: 191-198. DOI: 10.1016/j.fusengdes.2005.06.071
- [39] Faugel H, Angene P, Becker W, Braun F, Bobkov V, et al. The ASDEX upgrade ICRF system: Operational experience and developments. Fusion Engineering and Design. 2005;**74**: 319-324. DOI: 10.1016/j.fusengdes.2005.06.268
- [40] Yang H, Zhang XJ, Yuan S, Qin CM, et al. Experimental validation of the newly designed ICRF antenna on EAST. Private Communication
- [41] Vulliez K, Argouarch A, Bosia G, et al. Validation of the load-resilient ion cyclotron resonance frequency antenna concept on Tore Supra plasmas. Nuclear Fusion. 2008;**48**:065007. DOI: 10.1088/0029-5515/48/6/065007
- [42] Hillairet J, Mollard P, Colas L, Helou W, Urbanczyk G, et al. WEST actively cooled load resilient ion cyclotron resonance heating system results. Nuclear Fusion. 2021;**61**:096030. DOI: 10.1088/1741-4326/ac1759
- [43] Ragona R, Messiaen A. Conceptual study of an ICRH traveling-wave antenna system for low-coupling conditions as expected in DEMO.

Nuclear Fusion. 2016;**56**:076009.  
DOI: 10.1088/0029-5515/56/7/076009

[44] Pinsker RI, Prater R, Moeller CP, deGrassie JS, et al. Experiments on helicons in DIII-D—investigation of the physics of a reactor-relevant non-inductive current drive technology. Nuclear Fusion. 2018;**58**:106007. DOI: 10.1088/1741-4326/aad1f8

[45] Van Compernelle B, Brookman MW, Moeller CP, Pinsker RI, Garofalo AM, O'Neill R, et al. The high-power helicon program at DIII-D: Gearing up for first experiments. Nuclear Fusion. 2021; **61**(11):116034. DOI: 10.1088/1741-4326/ac25c0

[46] Ragona R, Batal T, Hillairet J, Messiaen A, et al. Progress on the design of a DEMO high power ICRH travelling wave antenna mock-up to be tested on WEST. AIP Conference Proceedings. 2020;**2254**:070014. DOI: 10.1063/5.0014215

[47] Stangeby PC. The Plasma Boundary of Magnetic Fusion Devices (1st ed.). Boca Raton: CRC Press. 2000. DOI: 10.1201/9780367801489

[48] Moritz J, Heuraux S, Gravier E, Lesur M, Brochard F, et al. Sheath size and Child–Langmuir law in one dimensional bounded plasma system in the presence of an oblique magnetic field: PIC results. Physics of Plasmas. 2021;**28**:083501. DOI: 10.1063/5.0055790

[49] Myra JR. A tutorial on radio frequency sheath physics for magnetically confined fusion devices. Journal of Plasma Physics. 2021;**87**(5): 905870504. DOI: 10.1017/S0022377821000878

[50] Colas L, Urbanczyk G, Goniche M, Hillairet J, Bernard J-M, Bourdelle C, et al. The geometry of the ICRF-induced

wave–SOL interaction. A multi-machine experimental review in view of the ITER operation. Nuclear Fusion. 2022; **62**(1):016014. DOI: 10.1088/1741-4326/ac35f9

[51] Colas L, Lu LF, Jacquot J, Tierens W, et al. SOL RF physics modelling in Europe, in support of ICRF experiments. EPJ Web of Conferences. 2017;**157**: 01001. DOI: 10.1051/epjconf/201715701001

[52] Myra JR, D'Ippolito DA. Resonance cone interaction with a self-consistent radio-frequency sheath. Physical Review Letters. 2008;**101**:195004. DOI: 10.1103/PhysRevLett.101.195004

[53] Zhang W, Bilato R, Bobkov VV, et al. Recent progress in modeling ICRF-edge plasma interactions with application to ASDEX upgrade. Nuclear Fusion. 2021. DOI: 10.1088/1741-4326/ac38c8

[54] Urbanczyk G, Zhang XJ, Colas L, Dumont R, Tierens W, et al. Metallic impurity content behavior during ICRH-heated L-mode discharges in EAST. Nuclear Fusion. 2020;**60**:126003. DOI: 10.1088/1741-4326/abae82

[55] Martin K, Gunn JP, Heuraux S, Colas L, Faudot E, Jacquot J. Measurement of sheath potential in RF-biased flux tubes using a retarding field analyzer in Tore Supra tokamak. Journal of Nuclear Materials. 2013;**438**: S509-S512. DOI: 10.1016/j.jnucmat.2013.01.105

[56] Corre Y, Firdaouss M, Colas L, Argouarch A, Guilhem D, Gunn J, et al. Characterization of heat flux generated by ICRH heating with cantilevered bars and a slotted box Faraday screen. Nuclear Fusion. 2012;**52**:103010. DOI: 10.1088/0029-5515/52/10/103010

- [57] Martin MJ, Gekelman W, Van Compernelle B, Pribyl P, Carter T. Experimental observation of convective cell formation due to a fast wave antenna in the large plasma device. *Physical Review Letters*. 2017;**119**:205002. DOI: 10.1103/PhysRevLett.119.205002
- [58] Ochoukov R, Whyte DG, Brunner D, D'Ippolito DA, et al. ICRF-enhanced plasma potentials in the SOL of Alcator C-Mod. *Plasma Physics and Controlled Fusion*. 2014;**56**:015004. DOI: 10.1088/0741-3335/56/1/015004
- [59] Wukitch SJ, LaBombard B, Lin Y, Lipschultz B, Marmor E, et al. ICRF specific impurity sources and plasma sheaths in Alcator C-Mod. *Journal of Nuclear Materials*. 2009;**390–391**: 951-954. DOI: 10.1016/j.jnucmat.2009.01.245
- [60] Wukitch SJ, Lipschultz B, Marmor E, Lin Y, et al. RF plasma edge interactions and their impact on ICRF antenna performance in Alcator C-Mod. *Journal of Nuclear Materials*. 2007;**363–365**:491-497. DOI: 10.1016/j.jnucmat.2007.01.273
- [61] Dux R, Bobkov V, Herrmann A, Janzer A, Kallenbach A, et al. Plasma-wall interaction and plasma behaviour in the non-boronised all tungsten ASDEX Upgrade. *Journal of Nuclear Materials*. 2009;**390–391**:858-863. DOI: 10.1016/j.jnucmat.2009.01.225
- [62] Bobkov V, Balden M, Bilato R, Braun F, et al. ICRF operation with improved antennas in ASDEX Upgrade with W wall. *Nuclear Fusion*. 2013;**53**: 093018. DOI: 10.1088/0029-5515/53/9/093018
- [63] Bobkov V, Aguiam D, Bilato R, Brezinsek S, Colas L, et al. Making ICRF power compatible with a high-Z wall in ASDEX upgrade. *Plasma Physics and Controlled Fusion*. 2017;**59**:014022. DOI: 10.1088/0741-3335/59/1/014022
- [64] Colas L, Jacquet P, Bobkov V, Brix M, Meneses L, et al. 2D mappings of ICRF-induced SOL density modifications on JET. In: 45th EPS Conference on Plasma Physics Proceedings. <http://ocs.ciemat.es/EPS2018PAP/pdf/O4.101.pdf>
- [65] Urbanczyk G, Colas L, Zhang XJ, Helou W, Hillairet J, et al. ICRH coupling optimization and impurity behavior in EAST and WEST. *AIP Conference Proceedings*. 2020;**2254**:030012. DOI: 10.1063/5.0018453
- [66] Tierens W, Colas L, EUROfusion MST1 Team. Slab-geometry surface waves on steep gradients and the origin of related numerical issues in a variety of ICRF codes. *Journal of Plasma Physics*. 2021;**87**(4):905870405. DOI: 10.1017/S002237782100074X
- [67] Tierens W, Zhang W, Manz P, et al. The importance of realistic plasma filament waveforms for the study of resonant wave-filament interactions in tokamak edge plasmas editors-pick *Physics of Plasmas*. 2020;**27**:052102. DOI: 10.1063/5.0007098
- [68] Perkins RJ, Hosea JC, et al. High-harmonic fast-wave power flow along magnetic field lines in the scrape-off layer of NSTX. *Physical Review Letters*. 2012;**109**:045001. DOI: 10.1103/PhysRevLett.109.045001
- [69] Noterdaeme JM. Fifty years of progress in ICRF, from first experiments on the model C stellarator to the design of an ICRF system for DEMO. *AIP Conference Proceedings*. 2020;**2254**: 020001. DOI: 10.1063/5.0014254
- [70] Van Eester D, Lerche E. Integro-differential modeling of ICRH wave

propagation and damping at arbitrary cyclotron harmonics and wavelengths in tokamaks. AIP Conference Proceedings. 2014;**1580**:298. DOI: 10.1063/1.4864547

[71] Dumont RJ. Variational approach to radiofrequency waves in magnetic fusion devices. Nuclear Fusion. 2009;**49**:075033. DOI: 10.1088/0029-5515/49/7/075033

[72] Brambilla M. Numerical simulation of ion cyclotron waves in tokamak plasmas. Plasma Physics and Controlled Fusion. 1999;**41**:1. DOI: 10.1088/0741-3335/41/1/002

[73] Bilato R, Volpe F, Poli E, Köhn A, et al. Electron Cyclotron Heating in RFP plasmas. AIP Conference Proceedings. 2009;**1187**:81. DOI: 10.1063/1.3273812

[74] Kazakov YO, Ongena J, Wright JC, et al. Physics and applications of three-ion ICRF scenarios for fusion research. Physics of Plasmas. 2021;**28**:020501. DOI: 10.1063/5.0021818

[75] Lin Y, Wright J, Wukitch S. Physics basis for the ICRF system of the SPARC tokamak. Journal of Plasma Physics. 2020;**86**(5):865860506. DOI: 10.1017/S0022377820001269

[76] Lerche E, Goniche M, Jacquet P, Van Eester D, Bobkov V, Colas L, et al. Optimization of ICRH for core impurity control in JET-ILW. Nuclear Fusion. 2016;**56**:036022. DOI: 10.1088/0029-5515/56/3/036022

[77] TFR Group. Impurity pump-out at the two-ion hybrid resonance during ICRF experiments in TFR tokamak plasmas. Nuclear Fusion. 1982;**22**:956

[78] Rice JE, Lin Y, Perks CJ, Reinke ML, et al. Argon pumpout by ICRF waves in C-Mod L- and I-mode plasmas. Nuclear Fusion. 62 086009; 2022. DOI: 10.1088/1741-4326/ac6ef0

[79] Wukitch S et al. Towards ICRF antennas compatible with high performance plasmas: characterization and mitigation of ICRF antenna – plasma edge interaction. In: 22<sup>nd</sup> RFPPC Conference. France: Aix-en-Provence; 2017

[80] Hillairet J. Recent progress in ion cyclotron range of frequency in magnetic confinement fusion. From modelling technology and experiments. Reviews of Modern Physics. 2022. (Under reviewing process)

# We are IntechOpen, the world's leading publisher of Open Access books Built by scientists, for scientists

6,300

Open access books available

171,000

International authors and editors

190M

Downloads

Our authors are among the

154

Countries delivered to

TOP 1%

most cited scientists

12.2%

Contributors from top 500 universities



WEB OF SCIENCE™

Selection of our books indexed in the Book Citation Index  
in Web of Science™ Core Collection (BKCI)

Interested in publishing with us?  
Contact [book.department@intechopen.com](mailto:book.department@intechopen.com)

Numbers displayed above are based on latest data collected.  
For more information visit [www.intechopen.com](http://www.intechopen.com)



## Chapter

# Charged Particle Beam Injection into Magnetically Confined Plasmas

*Wonyong Chung, Andi Tan and Christopher Tully*

## Abstract

As the principles underpinning magnetic confinement are contrary to allowing significant heat flow via charged particles into or out of a magnetically confined plasma, the approach of charged particle beam injection has been largely overlooked. The method of magnetic orbital angular momentum beam acceleration, developed by the PTOLEMY experiment, provides a new avenue for injecting charged particle beams into high magnetic field regions. Initial simulations show how this novel acceleration method can yield charge, mass, and heat flow into toroidal magnetic fields with important implications for fusion energy science. This chapter will review this new method in the context of charged particle beam injection methods and the relevance of these tools for plasma and fusion science.

**Keywords:** charged particle beam injection, heating, magnetic confinement, magnetic gradient drift, ITER

## 1. Introduction

The dream of harnessing energy from controlled nuclear fusion has been proposed for several decades. Intensifying climate change issues increase the desire for a clean and safe energy source. A fusion reactor based on magnetic confinement provides a promising configuration for controlled thermonuclear fusion. To fuse nuclei with large densities for an extended period, it is necessary to heat the plasma to overcome the Coulomb repulsion. The power ratio,  $Q$ , of the fusion output power to the input power is proportional to the fusion product  $nT\tau_E$ , where  $n$  and  $T$  are the central ion density and temperature [1]. The parameter  $\tau_E$  is the energy confinement time. In December 2021, the Joint European Torus (JET) achieved a new record and produced 59 MJ of energy with a  $Q$  of 0.33 over a  $\tau_E$  of 5 s [2]. Although remarkable progress has been made to achieve the required  $n$ ,  $T$ , and  $\tau_E$ , they have not been achieved in the same reactor configuration simultaneously.

To achieve an ignition condition where self-sustaining fusion is possible, additional energy-efficient heating is required. Ohmic heating from the toroidal current wanes at high temperatures. Two external sources are typically used to provide heating power, the resonant absorption of radio frequency electromagnetic waves and the injection of energetic neutral particle beams.

The injected beams are neutralized to prevent reflection due to the magnetic field. The neutralization process introduces inefficiency and complicates the instrumentation.

Alternatives to neutral particle beam injection, typically for non-equilibrium fusion reactors, have been explored using different acceleration technologies [3, 4]. The challenges of energy efficiency in particle acceleration are formidable given the high fraction of input power needed to operate relatively low- $Q$  fusion reactors. Radio-frequency acceleration cavities and time-varying electromagnetic fields are, in general, prone to internal ohmic losses and self-heating. Static accelerating fields avoid the bulk of these losses, but are suited primarily for charged particle beams. By construction, the insertion and extraction of charged particles from magnetic confinement systems is thwarted except when necessary, as in the case of divertors. However, non-confining trajectories can be constructed under special conditions through the same processes of cyclotron orbit drift that plague steady-state operation.

In the transverse drift electromagnetic filter developed for the PTOLEMY experiment (Princeton Tritium Observatory for Light, Early-Universe, Massive-Neutrino Yield), a compact configuration of electromagnetic fields simultaneously transports and decelerates energetic electrons from the tritium  $\beta$ -decay endpoint starting in high magnetic fields of several Tesla to regions where both the kinetic energy and magnetic fields are reduced by several orders of magnitude [5, 6]. A new method is devised to accelerate low-energy charged particles into a high magnetic field region by operating the PTOLEMY filter in “reverse.” This chapter presents the principles of this acceleration method and describes a possible application using the diagnostic port of the International Thermonuclear Experimental Reactor (ITER) [7].

## 2. Basics of charged particle beam injection

In this chapter, we use the convention that non-bolded symbols of vector quantities refer to the total magnitude unless a component is specified. The equation of motion of a charged particle of mass  $m$  and charge  $q$  in a magnetic field  $\mathbf{B}$  is given by

$$\frac{d}{dt} \left( m \frac{d\mathbf{r}}{dt} \right) = q \frac{d\mathbf{r}}{dt} \times \mathbf{B}. \quad (1)$$

The Lorentz force on the right-hand side is perpendicular to the particle’s velocity. In a uniform magnetic field, the particle’s motion projected on a plane perpendicular to the magnetic field is circular, with a gyroradius given by

$$\rho = \frac{mv_{\perp}}{qB} = \frac{\sqrt{2mT_{\perp}}}{qB}, \quad (2)$$

with  $T_{\perp}$  the transverse kinetic energy.

For a 1 MeV deuterium ion in a 5 T magnetic field, the gyroradius is about 0.04 m, a small fraction of a typical reactor radius. The ion beam injection energies must be relativistic to be commensurate with the reactor radius.

Relativistic ion beam injection introduces a number of inefficiencies. The plasma does not have the density required to stop energetic ions in a single transit, delivering limited power to the plasma and creating destructive irradiation of the reactor walls. The acceleration methods for relativistic beams involve time-varying fields that have several sources of intrinsic power loss.

In the following sections, charged particle injection of non-relativistic ions is re-examined as a transport mechanism that drifts charged ions from outside of the reactor volume to the surface of the plasma.

### 3. Magnetic orbital angular momentum beam acceleration

An alternative method to inject a charged particle beam is to create a beam of particles whose gyroradius is small compared to the transverse dimensions of the injection aperture. The particles are in cyclotron motion in a magnetic field that is relatively strong compared to their momentum. The acceleration mechanism stems from the ability of particles traveling in cyclotron motion in magnetic field gradients to do work. One, therefore, configures a magnetic geometry such that there is a transverse gradient along the average path of the beam. A complementary electric field is used to balance the gradient- $B$  drift transverse to the average path of the beam and to accelerate the particles under the work of the magnetic field gradient. The acceleration process will be shown to be adiabatic for relevant injection energies and to maintain the magnetic moment invariance to a good accuracy after an initial stage of zero field ion source injection. The acceleration process does not affect the average linear momentum component of the beam. The increase in the charged particle kinetic energy follows from an increase in the magnetic orbital angular momentum.

#### 3.1 Guiding-center drifts in adiabatic field conditions

When a charged particle gyrates in a magnetic field with a transverse gradient, the cyclotron-orbit averaged Guiding Center System (GCS) [8] motion can be described in terms of the drift terms of the virtual guiding-center particle if the spatial and temporal field variations within a single cyclotron orbit are taken to be adiabatic, i.e.,

$$\rho_c \ll \left| \frac{B}{\nabla B} \right|, \left| \frac{E}{\nabla E} \right|; \text{ and} \quad (3)$$

$$\tau_c \ll \left| \frac{B}{dB/dt} \right|, \left| \frac{E}{dE/dt} \right|; \quad (4)$$

where  $\rho_c$  is the Larmor radius and  $\tau_c$  the cyclotron period. Under the conditions specified by Eq. (3) and (4), the first adiabatic invariant  $\mu$ ,

$$\mu = \frac{mv_{\perp}^2}{2B} = \frac{T_{\perp}}{B}, \quad (5)$$

accurately describes an invariant quantity preserved in the motion of the particle [9, 10] and shows that an increase in the magnetic field magnitude is accompanied by a proportional increase in the transverse kinetic energy. Additionally, the deviation of the GCS trajectory from the direction of the magnetic field lines can be described in terms of four fundamental drift terms,

$$\mathbf{V}_D = \mathbf{V}_{\perp} = \left( q\mathbf{E} + \mathbf{F} - \mu\nabla B - m \frac{d\mathbf{V}}{dt} \right) \times \frac{\mathbf{B}}{qB^2}, \quad (6)$$

where  $V_{\perp}$  is the perpendicular component of the GCS velocity with respect to the magnetic field line. The transverse drift velocity,  $V_D$ , is composed of individual terms, as appear in Eq. (6) from left to right, known as (1) the  $E \times B$  drift; (2) the external force drift; (3) the gradient- $B$  drift; and (4) the inertial drift [8]. It is possible to configure the electric and magnetic field parameters to manipulate certain drift terms to produce a net linear trajectory in the transverse direction [5].

### 3.2 Drifts and work

The gradient- $B$  drift is able to drive a charged particle up or down an electrostatic potential. This ability to do work, at first, seems contrary to the notion that magnetic fields do not do work on charged particles, as seen in Eq. (1), from the cross-product. Similarly, under the motion of  $E \times B$  drift alone, the cross-product bars work as the electrons will drift on surfaces of constant voltage. This can also be understood by considering that it is always possible to boost into a frame in which the  $E \times B$  drift is zero.

In contrast, a gradient- $B$  drift due to a spatially varying magnetic field implies a time-varying electric field that cannot be boosted to zero. By itself, i.e., with a magnetic field and no electric field, a gradient- $B$  does no work because there is nothing to do work against. However, when accompanied by an external  $E \times B$  drift, the external electric potential provides a surface against which the gradient- $B$  drift can do work on. The internal rotational kinetic energy of gyromotion of the virtual guiding-center particle is reduced for a corresponding increase in voltage potential. This is described by inserting terms from Eq. (6),

$$\frac{dT_{\perp}}{dt} = -q\mathbf{E} \cdot \mathbf{V}_D = -q\mathbf{E} \cdot (q\mathbf{E} - \mu\nabla B) \times \frac{\mathbf{B}}{qB^2} = \frac{\mu}{B^2} \mathbf{E} \cdot (\nabla B \times \mathbf{B}), \quad (7)$$

where  $T_{\perp}$  is the internal kinetic energy of gyromotion in the GCS frame [8].

### 3.3 Balanced drift

To produce a filter or accelerator based on the drift terms in Eq. (6), the external force and inertial drift terms are first taken to be zero, leaving only the electric and gradient- $B$  drifts to be configured such that the total net drift is along a straight line parallel to the direction of the magnetic field gradient. The gradient- $B$  drift alone is orthogonal to the direction of the magnetic field gradient, so the first step is to create a component of the  $E \times B$  drift that exactly counters the gradient- $B$  drift. From Eq. (6), this specifies the requirement,

$$q\mathbf{E}_{\parallel} \times \mathbf{B} = \mu\nabla B \times \mathbf{B}, \quad (8)$$

where  $E_{\parallel}$  is the component of electric field parallel to the magnetic field gradient. In general, the ratio of the parallel electric field to the magnitude of the magnetic field to meet this condition depends on the ratio  $\mu/q$  times the fractional rate of change of the transverse component of the magnetic field along the direction of the magnetic field gradient. For an exponentially falling transverse field, the fractional rate of change is  $1/\lambda$ , the characteristic exponential length scale in units of transverse distance.

To introduce work, the electric field is tilted by adding an additional component,  $E_{\perp}$ , that is orthogonal to the direction of the magnetic field gradient. The  $E_{\perp} \times B$  drift is what moves the charged particle either against or along the magnetic field gradient. As the components of  $E_{\parallel}$  and  $E_{\perp}$  are in vacuum, the relationship between the components follows from solving Maxwell's equations for a set of voltage plates above and below the direction of the balanced drift. Explicit solutions have been found [5]. Given that the magnitudes of  $E_{\parallel}$  and  $E_{\perp}$  are related, it is not surprising that the net drift velocity along the acceleration direction is constant. There is no linear momentum acceleration present. The acceleration occurs through the increase in the transverse kinetic energy component, the magnetic orbital angular momentum, during a process of constant drift along the magnetic field gradient.

### 3.4 Performance

Because the orbital magnetic moment  $\mu = T_{\perp}/B$  is invariant, if the  $B$  field increases (or decreases) exponentially along the trajectory of the particle, so must its transverse kinetic energy. **Figure 1** shows the trajectory of a deuterium ion in a balanced drift with an initial kinetic energy of 20 keV at 0.2 T, going to a 4.7 T region with 1 MeV final kinetic energy. In this simulation, using CST studio [11], the magnetic field (**Figure 2**) is scaled from the one produced by the PTOLEMY magnet [6]. The maximum of the  $B_x$  field is set to 4.7 T at  $Z = 1.6$  m to match the toroidal field near the interface of the upper port of ITER [12]. The electric field as in **Figure 3** is generated by a similar electrode structure as in the PTOLEMY transverse drift filter [6]. The dimensions are scaled up such that the distance between the electrodes is 0.3 m.

### 3.5 Injection

The net drift is along the direction of the magnetic field gradient and drives the guiding-center of the beam to cross equipotential lines and accelerates the particles. As the beam drifts in the direction of  $\nabla B$ , it naturally reaches its maximum kinetic energy upon entering the toroidal magnet of a tokamak.

Via the foregoing mechanism, initial simulations of injecting deuterium ions indicate successful delivery of the beam, as shown in **Figure 4**. Once the particle leaves

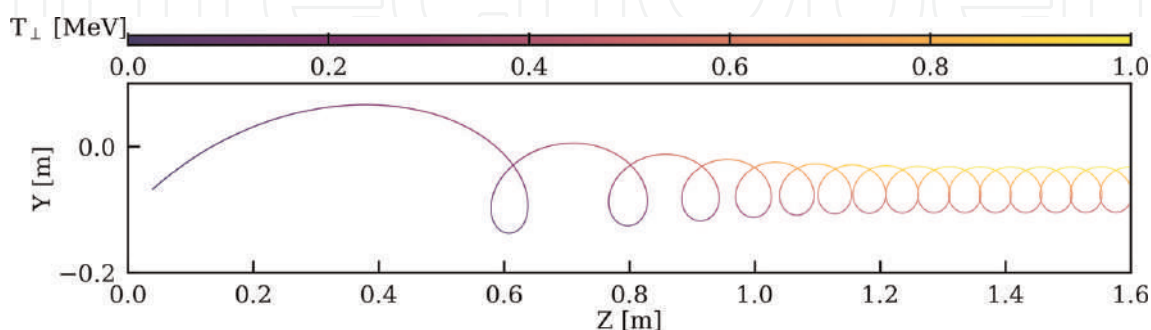


**Figure 1.** The trajectory of a deuterium ion in a transverse drift accelerator is shown with the low energy ion source on the left at a low magnetic field region and the high energy ion exiting the accelerator on the right in a region of high magnetic field. The net vertical drift is balanced to zero by construction as the ion drifts at constant velocity from left to right while climbing the magnetic field gradient. The trajectory is computed using the CST software suite. The color scale indicates the kinetic energy of the ion increasing from 20 keV at 0.2 T to 1 MeV at 4.7 T.

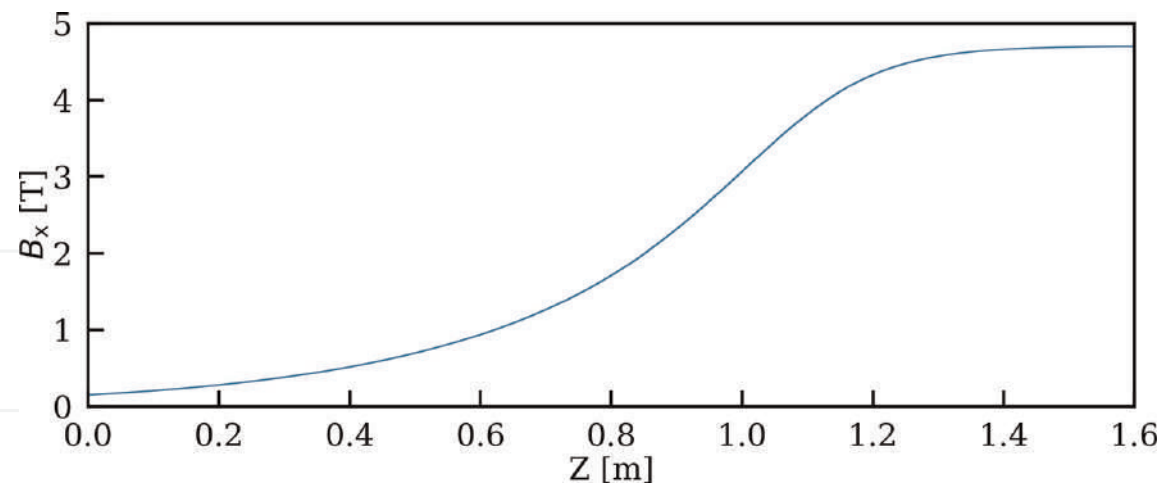


**Figure 2.**  
The profile of the transverse magnetic field in the CST simulation for the trajectory shown in **Figure 1**. It is derived from scaling the magnetic field produced by the PTOLEMY magnet to match a maximum  $B_x$  of 4.7 T.

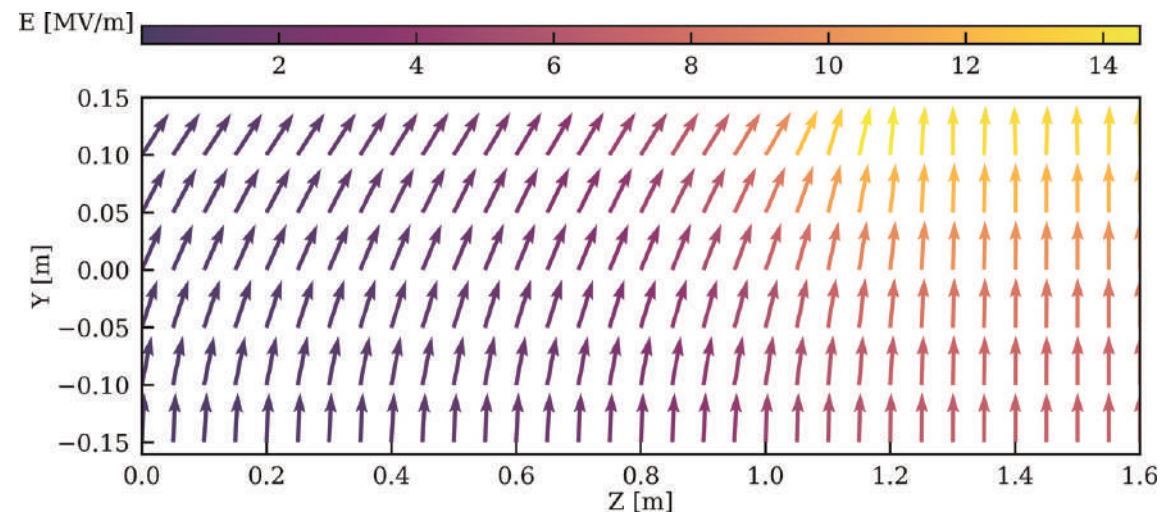


**Figure 3.**  
The electric field in the transverse plane in the drift region for the trajectory shown in **Figure 1**. The color (orientation) of the arrow indicates the magnitude (direction) of the field at its tail-end position.

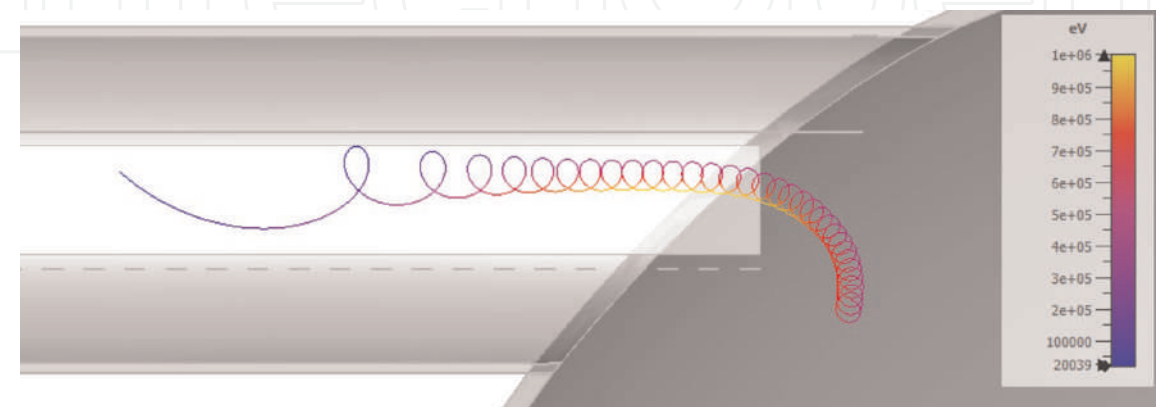


**Figure 4.**  
Simulation of the injection of deuterium ions into a  $1/R$  magnetic field in a tokamak using the accelerating structure of **Figure 1**. Upon exiting the accelerator, the energetic ion continues to drift toward the plasma confinement region under the  $1/R$  magnetic field gradient-B drift of the tokamak.

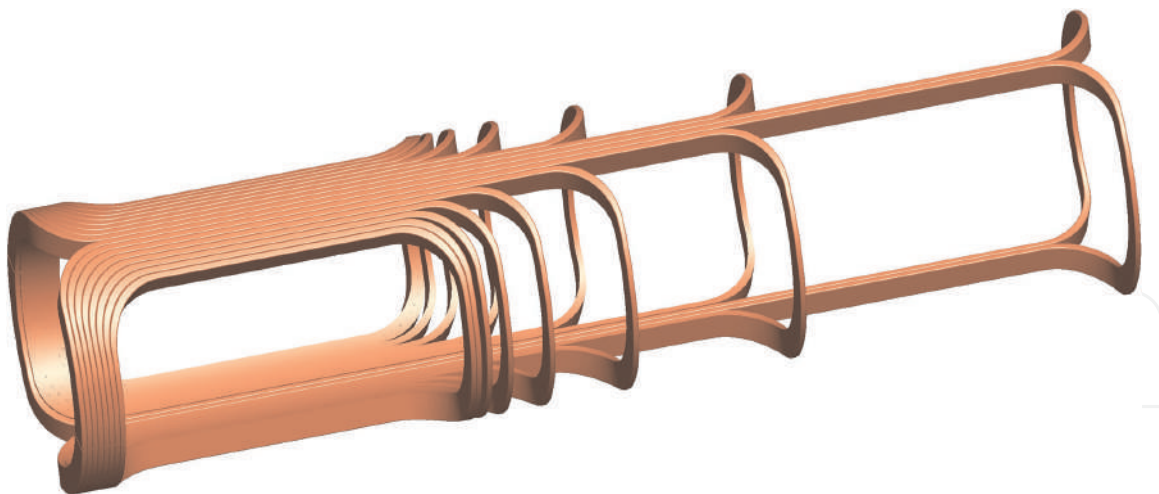


**Figure 5.**  
*A conceptual design of a tapered dipole magnet winding to generate the desired magnetic field for magnetic orbital angular momentum beam acceleration. The winding of the coils follows the surface of a cylindrical vacuum insertion port, similar to dipole magnets used in circular proton beam accelerators.*

the injection port, the gradient of the  $1/R$  toroidal magnetic field drifts the ions into the center of the plasma. The relatively hot thermal temperature of the 1 MeV deuterium ions will thermalize through Coulomb interactions with the plasma. The injection mechanism supports a range of injection energies and ion species. For instance, injection of 4 MeV  $\alpha$ -particles through the ITER diagnostic port may be an effective way of studying the effects of fusion final-state ion interactions on the plasma. Charge neutralization can be achieved by instrumenting ion (electron) injection ports on the top (bottom) of the tokamak. The gradient- $B$  drift will drift ions downward (for a given orientation of the azimuthal toroidal magnetic field) and electrons (or negative ions) upward.

The desired injection magnetic field, as described in Ref. [6], can be produced by a tapered dipole magnet with a superconductor winding, as in **Figure 5**.

A field cage with a number of electrodes can be placed inside the magnet to produce the corresponding electric field. Such a magnet is compact and can be placed within a counter-dipole coil in the upper diagnostic ports of ITER, as shown in **Figure 6**. The counter-dipole creates a zero field region for the ion source and reduces Lorentz forces on the primary reactor coils. The details of this magnet and the field cage are beyond the scope of this chapter.

## 4. Energy efficiency

An important aspect of magnetic orbital angular momentum acceleration for fusion energy efficiency is the reliance solely on static electric and magnetic fields. The power loading during injection on the accelerating plate voltages draws from highly efficient DC power supplies. Above all, the largest inefficiency of neutral beam injection, the neutralization, is avoided with direct charged particle injection. The high currents and efficient production of positive ions saves on power losses at the source relative to the negative ion beams used for neutral beam injection [13]. The inefficiencies and beam energy limitations associated with neutralization and

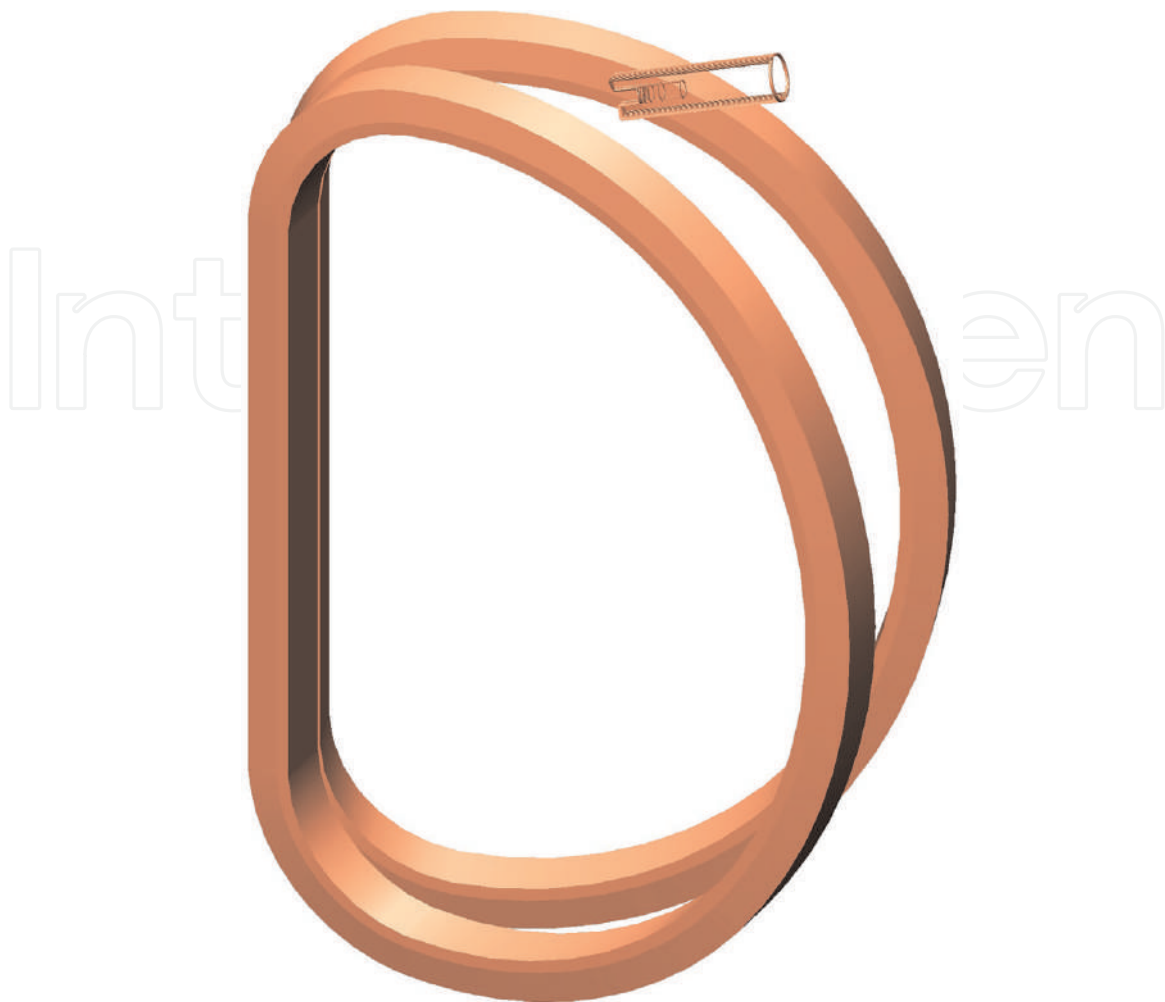


**Figure 6.**

*A tapered dipole magnet, as shown in Figure 5, within a counter-dipole winding placed in the upper port between two adjacent ITER toroidal field coils. The counter-dipole reduces the magnetic forces between the injection system and the tokamak field windings.*

neutral beam injection introduce approximately a factor of 2 loss in absolute power efficiency [14].

## 5. Conclusions

Fusion reactor science is on the brink of a major advance toward sustained clean energy reactors. Reducing inefficiency in the particle beam injection systems is a promising direction toward achieving ignition conditions without compromising reactor operation. A surprising and yet potentially revolutionary approach to improving beam heating is through a new particle acceleration method called magnetic orbital angular momentum beam acceleration. With this technique, charged particle beam injection into magnetically confined plasmas becomes possible. The relevant parameters for charged particle beam injection are presented with simulated geometries demonstrating the feasibility of implementing this system with the diagnostic port of ITER. Charged particle beam injection provides a new tool for fusion reactors to deliver charge, mass, and heat flow into the plasma. The large gain in energy efficiency for charged particle injection is the most advantageous factor in comparing with neutral beam injection.

## Acknowledgements

This research was supported by the Simons Foundation (#377485) and the John Templeton Foundation (#61814).

IntechOpen

IntechOpen


## Author details

Wonyong Chung, Andi Tan\* and Christopher Tully  
Department of Physics, Princeton University, Princeton, New Jersey, USA

\*Address all correspondence to: [andit@princeton.edu](mailto:andit@princeton.edu)

## IntechOpen

---

© 2022 The Author(s). Licensee IntechOpen. This chapter is distributed under the terms of the Creative Commons Attribution License (<http://creativecommons.org/licenses/by/3.0>), which permits unrestricted use, distribution, and reproduction in any medium, provided the original work is properly cited. 

## References

- [1] Wesson J, Campbell DJ. Tokamaks. Oxford, England: Oxford University Press; 2011. Available online: <https://global.oup.com/academic/product/tokamaks-9780199592234>
- [2] Gibney E. Nuclear-fusion reactor smashes energy record. *Nature*. 2022; **602**(7897):371-371
- [3] Liu KF, Chao AW. Accelerator based fusion reactor. *Nuclear Fusion*. 2017; **57**(8):084002
- [4] Labaune C, Baccou C, Depierreux S, Goyon C, Loisel G, Yahia V, et al. Fusion reactions initiated by laser-accelerated particle beams in a laser-produced plasma. *Nature Communications*. 2013; **4**(1):1-6
- [5] Betti MG, Biasotti M, Bosca A, Calle F, Carabe-Lopez J, Cavoto G, et al. A design for an electromagnetic filter for precision energy measurements at the tritium endpoint. *Progress in Particle and Nuclear Physics*. 2019; **106**:120-131
- [6] Apponi A, Betti MG, Borghesi M, Canci N, Cavoto G, Chang C, et al. Implementation and optimization of the PTOLEMY transverse drift electromagnetic filter. *Journal of Instrumentation*. 2022; **17**(05):P05021. DOI: 10.1088/1748-0221/17/05/p05021
- [7] International Thermonuclear Experimental Reactor (ITER). 2022. Available from: <http://www.iter.org> [Accessed: 2022-06]
- [8] Roederer J, Zhang H. Particle fluxes, distribution functions and violation of invariants. In: *Dynamics of Magnetically Trapped Particles*. Berlin, Heidelberg: Springer-Verlag; 2014. pp. 89-122. Available online: <https://link.springer.com/book/10.1007/978-3-642-41530-2>
- [9] Alfvén H. On the motion of a charged particle in a magnetic field. *Arkiv för Matematik, Astronomi, och Fysik*. 1940; **25B**(1-20):29
- [10] Cary JR, Brizard AJ. Hamiltonian theory of guiding-center motion. *Reviews of Modern Physics*. 2009; **81**(2):693
- [11] Dassault Systèmes. CST Studio Suite; Available from: <http://www.cst.com>
- [12] International Atomic Energy Agency. Summary of the ITER Final Design Report. No. 22 in ITER EDA Documentation Series. Vienna: International Atomic Energy Agency; 2001. Available from: <https://www.iaea.org/publications/6442/summary-of-the-iter-final-design-report>
- [13] Hemsworth RS, Inoue T. Positive and negative ion sources for magnetic fusion. *IEEE Transactions on Plasma Science*. 2005; **33**(6):1799-1813
- [14] Hopf C, Starnella G, den Harder N, Fantz U. Neutral beam injection for fusion reactors: Technological constraints versus functional requirements. *Nuclear Fusion*. 2021; **61**(10):106032. DOI: 10.1088/1741-4326/ac227a

# We are IntechOpen, the world's leading publisher of Open Access books Built by scientists, for scientists

6,300

Open access books available

171,000

International authors and editors

190M

Downloads

Our authors are among the

154

Countries delivered to

TOP 1%

most cited scientists

12.2%

Contributors from top 500 universities



WEB OF SCIENCE™

Selection of our books indexed in the Book Citation Index  
in Web of Science™ Core Collection (BKCI)

Interested in publishing with us?  
Contact [book.department@intechopen.com](mailto:book.department@intechopen.com)

Numbers displayed above are based on latest data collected.  
For more information visit [www.intechopen.com](http://www.intechopen.com)



# Decoupling Techniques for Coupled PDE Models in Fluid Dynamics

*Mingchao Cai, Mo Mu and Lian Zhang*

## Abstract

We review decoupling techniques for coupled PDE models in fluid dynamics. In particular, we are interested in the coupled models for fluid flow interacting with porous media flow and the fluid structure interaction (FSI) models. For coupled models for fluid flow interacting with porous media flow, we present decoupled preconditioning techniques, two-level and multilevel methods, Newton-type linearization-based two-level and multilevel algorithms, and partitioned time-stepping methods. The main theory and some numerical experiments are given to illustrate the effectiveness and efficiency of these methods. For the FSI models, partitioned time-stepping algorithms and a multirate time-stepping algorithm are carefully studied and analyzed. Numerical experiments are presented to highlight the advantages of these methods.

**Keywords:** decoupling, linearization, Stokes/Darcy model, FSI model, finite element, two-level method, Robin-Neumann scheme,  $\beta$ -scheme

## 1. Introduction

Coupled PDE models have wide applications in the real world. For example, in fluid dynamics, there are two-phase flow models, fluid structure interaction models, heat transfer models in fluids etc. In this work, we focus on two typical models: coupled models for describing fluid flow interacting with porous media flow, and fluid structure interaction (FSI) models. The first type of models have been validated by experiments [1] and then justified by using homogenization theory [2, 3]. Applications include the environmental engineering problem of groundwater contamination through rivers and the geoscience problem of surface flows filtrating in vuggy porous media. The second type of models come from many practical applications. For example, blood flow interacting with vessel wall, compressible fluids interacting with aircraft wings, as well as slamming and whipping response of ship structure to water flow. These models are typical multidomain coupled PDE models with multiphysics. Due to the heterogeneities in subdomain models, it is very difficult to find a unified approach to solve the different subdomain models simultaneously. Moreover, some

coupled models have nonlinearity in either subdomain problems or interface coupling terms. To deal with the difficulties caused by the coupling of different submodels and the nonlinearity [4–8], we discuss some decoupling techniques [4, 9–20], which have shown to be very effective and efficient. Among them, we will emphasize the work proposed by our group members and highlight the novelty and importance of these algorithms.

The rest of the paper is organized as follows. In Section 2, we introduce the coupled fluid flow/porous media interacting models. Some decoupling techniques, specifically, decoupled preconditioners, decoupled two-level and multi-level methods, and partitioned time schemes will be presented and analyzed. In Section 3, we present fluid structure interaction models. Partitioned decoupling algorithms include the Robin-Neumann scheme [14, 15], the  $\beta$ -scheme [13, 21], and the multirate partitioned schemes [22, 23] will be briefly introduced. Concluding remarks are drawn in Section 4.

## 2. Decoupled algorithms for the coupled models of fluid flow interacting with porous flow

For the linear cases of the coupled models for fluid flow interacting with porous media flow, we refer to the Stokes/Darcy model studied in [7, 11, 18, 20, 24–30]. For the nonlinear case, we refer to the coupled nonlinear Navier–Stokes/Darcy model [4–6].

### 2.1 Coupled models for fluid flow interacting with porous media flow

Let  $\Omega \subset R^d$  be a domain consisting of a fluid region  $\Omega_f$  and a porous media region  $\Omega_p$  separated by an interface  $\Gamma$ , as shown in **Figure 1**, where  $d = 2$  or  $3$ ,  $\Omega = \Omega_f \cup \Omega_p$  and  $\Gamma = \overline{\Omega_f} \cap \overline{\Omega_p}$ . Let  $\mathbf{n}_f$  and  $\mathbf{n}_p$  denote the unit outward normal directions on  $\partial\Omega_f$  and  $\partial\Omega_p$ . The interface  $\Gamma$  is assumed to be smooth enough as in [6].

For incompressible Newtonian fluid flow, Navier–Stokes equations of the stress-divergence form are usually used [31, 32].  $\forall t \geq 0, \forall \mathbf{x} \in \Omega_f$ ,

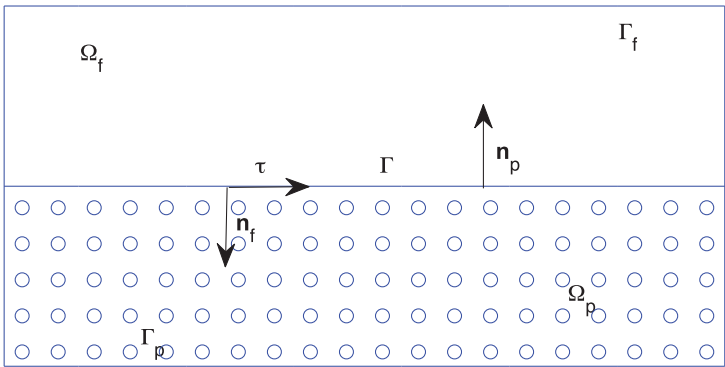


**Figure 1.** A global domain  $\Omega$  consisting of a fluid region  $\Omega_f$  and a porous media region  $\Omega_p$  separated by an interface  $\Gamma$ .

$$\begin{cases} \rho_f \left( \frac{\partial \mathbf{u}}{\partial t} + (\mathbf{u} \cdot \nabla) \mathbf{u} \right) - \operatorname{div} \mathbf{T}(\mathbf{u}, p) = \mathbf{f}_f, \\ \operatorname{div} \mathbf{u} = 0, \end{cases} \quad (1)$$

where  $\rho_f$  is the fluid density,  $\mathbf{u}$  is the velocity vector,  $p$  is the pressure,  $\mathbf{f}_f$  is the external force,

$$\mathbf{T}(\mathbf{u}, p) = 2\nu \mathbf{D}(\mathbf{u}) - p\mathbf{I}, \quad \text{with} \quad \mathbf{D}(\mathbf{u}) = \frac{1}{2} [\nabla \mathbf{u} + (\nabla \mathbf{u})^T], \quad (2)$$

is the stress tensor with  $\nu > 0$  being the kinematic viscosity. By dropping the term  $\frac{\partial \mathbf{u}}{\partial t}$  in (1), the steady state Navier–Stokes equations read as:  $\forall \mathbf{x} \in \Omega_f$ ,

$$\begin{cases} \rho_f (\mathbf{u} \cdot \nabla) \mathbf{u} - \operatorname{div} \mathbf{T}(\mathbf{u}, p) = \mathbf{f}_f, \\ \operatorname{div} \mathbf{u} = 0. \end{cases} \quad (3)$$

In strong form,

$$-\operatorname{div} \mathbf{T}(\mathbf{u}, p) = -\nu \Delta \mathbf{u} + \nabla p, \quad (4)$$

because the fluid flow is assumed to be divergence free and  $\operatorname{div} (\nabla^T \mathbf{u}) = 0$  holds.

Among various porous media flow models, Darcy's law is the most favored. The governing variable in  $\Omega_p$  is the so-called *piezometric head* or *pressure head*,

$$\phi = z + \frac{p_p}{\rho_f g}. \quad (5)$$

Here,  $z$  is the elevation from a reference level (for simplicity,  $z$  is assumed to be 0). Darcy's law states that the velocity  $\mathbf{u}_p$  (also called seepage velocity) in the porous media region is proportional to the gradient of  $\phi$  [27, 33].

$$\mathbf{u}_p = -K \nabla \phi. \quad (6)$$

We assume that

$$\alpha_1(\mathbf{x}, \mathbf{x}) \leq (K \mathbf{x}, \mathbf{x}) \leq \alpha_2(\mathbf{x}, \mathbf{x}), \quad \forall \mathbf{x} \in \Omega_p. \quad (7)$$

Moreover, the divergence of the seepage velocity equals to the source term. This leads to the following steady state equation:

$$-\operatorname{div} (K \nabla \phi) = f_p. \quad (8)$$

In the time-dependent case, the governing equations in  $\Omega_p$  reads as:

$$S_0 \phi_t - \operatorname{div} (K \nabla \phi) = f_p, \quad (9)$$

where  $S_0$  is a specific storage and  $f_p$  is a source term.

No matter time-dependent or steady state, the key part of the coupled model is a set of interface conditions, which describe the interaction mechanism of the two

different types of flows. The following interface conditions have been extensively used and studied in the literature [1–3, 7, 27, 28]:

$$\begin{cases} \mathbf{u} \cdot \mathbf{n}_f = \mathbf{u}_p \cdot \mathbf{n}_f = -K \nabla \phi \cdot \mathbf{n}_f, \\ -\nu (\nabla \mathbf{u}_f) \cdot \mathbf{n}_f + p = \rho g \phi, \\ -\nu (\nabla \mathbf{u}_f) \cdot \boldsymbol{\tau}_i = \frac{\nu \alpha_{BJS}}{\sqrt{\nu \boldsymbol{\tau}_i \cdot \mathbf{K} \boldsymbol{\tau}_i}} \mathbf{u} \cdot \boldsymbol{\tau}_i, \quad i = 1, \dots, d-1. \end{cases} \quad (10)$$

Here,  $\{\boldsymbol{\tau}_i\}_{i=1}^{d-1}$  is the unit tangent vector on  $\Gamma$ ,  $\alpha_{BJS}$  is a positive parameter depending on the properties of the porous medium. The first interface condition ensures mass conservation across  $\Gamma$ . The second one is the balance of normal forces across the interface. The third condition is well known as Beavers-Joseph-Saffman's law [1, 2], which states that the slip velocity is proportional to the shear stress along  $\Gamma$ . Without loss of generality, we impose homogeneous Dirichlet boundary conditions on both of the external boundaries:

$$\begin{cases} \mathbf{u} = \mathbf{0} & \text{on } \Gamma_f, \\ \phi = 0 & \text{on } \Gamma_p. \end{cases} \quad (11)$$

The proper functional spaces for  $\mathbf{u}$ ,  $p$  and  $\phi$  are

$$\begin{aligned} \mathbf{X}_f &= \left\{ \mathbf{v} \in \mathbf{H}^1(\Omega_f) = (H^1(\Omega_f))^d \mid \mathbf{v} = \mathbf{0} \text{ on } \Gamma_f \right\}, \\ Q &= L^2(\Omega_f), \quad X_p = \left\{ \psi \in H^1(\Omega_p) \mid \psi = 0 \text{ on } \Gamma_p \right\}. \end{aligned} \quad (12)$$

Moreover, we denote  $\underline{X} = \mathbf{X}_f \times X_p$  for ease of presentation. Multiplying test functions to (3) and (8), integrating by parts and plugging in the interface boundary conditions (10)–(11), we have the weak form of the coupled Navier–Stokes/Darcy model: find  $\underline{u} = (\mathbf{u}, \phi) \in \underline{X}$ ,  $p \in Q$  such that

$$\begin{cases} a(\underline{u}, \underline{v}) + c(\mathbf{u}, \mathbf{u}, \mathbf{v}) + b(\mathbf{v}, p) = f(\underline{v}) & \forall \underline{v} = (\mathbf{v}, \psi) \in \underline{X}, \\ b(\mathbf{u}, q) = 0 & \forall q \in Q, \end{cases} \quad (13)$$

where

$$\begin{aligned} a(\underline{u}, \underline{v}) &= a_f(\mathbf{u}, \mathbf{v}) + a_p(\phi, \psi) + a_\Gamma(\underline{u}, \underline{v}), \quad b(\mathbf{v}, p) = - \int_{\Omega_f} p \nabla \cdot \mathbf{v}, \\ c(\mathbf{u}, \mathbf{v}, \mathbf{w}) &= \rho \int_{\Omega_f} (\mathbf{u} \cdot \nabla) \mathbf{v} \cdot \mathbf{w}, \quad f(\underline{v}) = \int_{\Omega_f} \mathbf{f}_f \cdot \mathbf{v} + \rho g \int_{\Omega_p} f_p \psi \end{aligned} \quad (14)$$

with

$$\begin{aligned} a_f(\mathbf{u}, \mathbf{v}) &= \nu \int_{\Omega_f} \nabla \mathbf{u} : \nabla \mathbf{v} + \sum_{i=1}^{d-1} \frac{\nu \alpha_{BJS}}{\sqrt{\nu \boldsymbol{\tau}_i \cdot \mathbf{K} \boldsymbol{\tau}_i}} \int_{\Gamma} (\mathbf{u} \cdot \boldsymbol{\tau}_i)(\mathbf{v} \cdot \boldsymbol{\tau}_i), \\ a_p(\phi, \psi) &= \rho g \int_{\Omega_p} \nabla \psi \cdot \mathbf{K} \nabla \phi, \quad a_\Gamma(\underline{u}, \underline{v}) = \rho g \int_{\Gamma} (\phi \mathbf{v} - \psi \mathbf{u}) \cdot \mathbf{n}_f. \end{aligned} \quad (15)$$

For the wellposedness of the coupled Navier–Stokes/Darcy model, we refer to the recent results in [5, 6, 34]. It is shown in [34] that if the viscosity is sufficiently large and the normal velocity across the interface is sufficiently small, then the problem (14) is wellposed. We follow the assumptions in [34]. In addition to these assumptions on model parameters and variables, we shall frequently use these properties:  $a(\cdot, \cdot)$  is bounded and coercive;  $b(\cdot, \cdot)$  is bounded and satisfies the inf-sup condition [27, 35]; and the nonlinear term can be bounded by using the  $H^1$  norm of the three components [31, 36].

We partition  $\Omega_f$  and  $\Omega_p$  by quasi-uniform triangulations  $\mathcal{T}_{f,h}$  and  $\mathcal{T}_{p,h}$  with a characteristic meshsize  $h$ . Here, we require that the two subdomain triangulations coincide at  $\Gamma$ . The corresponding finite element spaces are denoted by  $\mathbf{X}_{f,h} \times Q_h \subset \mathbf{X}_f \times Q$  and  $X_{p,h} \subset X_p$ , respectively. Moreover,  $\mathbf{X}_{f,h} \times Q_h$  needs to be stable, i.e., there exists a positive constant  $\beta$  such that

$$\sup_{\mathbf{v}_h \in \mathbf{X}_{f,h}} \frac{b(\mathbf{v}_h, q_h)}{|\mathbf{v}_h|_{1,\Omega_f}} \geq \beta \|q_h\|_{0,\Omega_f} \quad \forall q_h \in Q_h. \quad (16)$$

We assume that the solution of (13) is smooth enough and the finite element spaces have the following typical approximation properties: for all  $(\mathbf{u}, p) \in \mathbf{H}^{k+1}(\Omega_f) \cap \mathbf{X}_f \times H^k(\Omega_f)$  and  $\phi \in H^{k+1}(\Omega_p) \cap X_p$ ,

$$\inf_{\mathbf{v}_h \in \mathbf{X}_{f,h}, q_h \in Q_h} \left\{ h|\mathbf{u} - \mathbf{v}_h|_{1,\Omega_f} + \|\mathbf{u} - \mathbf{v}_h\|_{0,\Omega_f} + h\|p - q_h\|_{0,\Omega_f} \right\} \lesssim h^{k+1} \left( |\mathbf{u}|_{k+1,\Omega_f} + |p|_{k,\Omega_f} \right), \quad (17)$$

$$\inf_{\psi_h \in X_{p,h}} \left\{ h|\phi - \psi_h|_{1,\Omega_p} + \|\phi - \psi_h\|_{0,\Omega_p} \right\} \lesssim h^{k+1} |\phi|_{k+1,\Omega_p}. \quad (18)$$

To satisfy the discrete inf-sup condition and the approximation properties (17)–(18), if  $k = 1$ , one may apply the Mini elements [31, 37] in  $\Omega_f$  and the piecewise linear elements in  $\Omega_p$ ; if  $k \geq 2$ , the  $k$ -th order Taylor-Hood elements [31, 37, 38] can be applied in  $\Omega_f$  and the piecewise  $k$ -th order elements can be adopted in  $\Omega_p$ .

**Coupled Algorithm:** A conventional finite element discretization applied to the model problem (13) leads to the discrete problem: Find  $\underline{\mathbf{u}}_h = (\mathbf{u}_h, \phi_h) \in \underline{\mathbf{X}}_h = \mathbf{X}_{f,h} \times X_{p,h}$ ,  $p_h \in Q_h$  such that

$$\begin{cases} a(\underline{\mathbf{u}}_h, \underline{\mathbf{v}}_h) + c(\mathbf{u}_h, \mathbf{u}_h, \mathbf{v}_h) + b(\mathbf{v}_h, p_h) = f(\underline{\mathbf{v}}_h) & \forall \underline{\mathbf{v}}_h = (\mathbf{v}_h, \psi_h) \in \underline{\mathbf{X}}_h, \\ b(\mathbf{u}_h, q_h) = 0, & \forall q_h \in Q_h. \end{cases} \quad (19)$$

## 2.2 Decoupled algorithms in the preconditioning steps

As an illustration of decoupled preconditioning techniques, we will consider the linear Stokes/Darcy model, whose weak form is (19) while the nonlinear term is dropped. We note that the discrete model in the operator form is

$$\begin{bmatrix} A_p & A_\Gamma^T & \mathbf{0} \\ -A_\Gamma & A_f & B_f^T \\ \mathbf{0} & B_f & \mathbf{0} \end{bmatrix} \begin{bmatrix} \phi_h \\ \mathbf{u}_h \\ p_h \end{bmatrix} = \begin{bmatrix} \mathbf{f}_{f,h} \\ \mathbf{f}_{p,h} \\ g_h \end{bmatrix}. \quad (20)$$

Here  $A_f, A_p, A_\Gamma$ , and  $B = (\mathbf{0}, B_f)$  are the corresponding linear operators induced by the corresponding bilinear forms in (15) and (16). We denote

$$A = \begin{bmatrix} A_p & A_\Gamma^T \\ -A_\Gamma & A_f \end{bmatrix}, \quad \text{and} \quad M = \begin{bmatrix} A & B^T \\ B & \mathbf{0} \end{bmatrix}. \quad (21)$$

By discarding the coupling interface terms and plugging in  $\frac{1}{\nu}I$  (which leads to pressure mass matrix) in the (2, 2) block, we have the following block-diagonal decoupled preconditioner:

$$P_M = \begin{bmatrix} A_0 & \mathbf{0} \\ \mathbf{0} & \frac{1}{\nu}I_h \end{bmatrix}, \quad \text{with} \quad A_0 = \begin{bmatrix} A_p & \mathbf{0} \\ \mathbf{0} & A_f \end{bmatrix}. \quad (22)$$

By keeping one of  $B$  and  $B^T$ , one can easily construct block-triangular decoupled preconditioner. GMRES method is used as the outer iterative method. Block diagonal or block-triangular preconditioners are used in the inner iteration. The effectiveness and the efficiency of the preconditioners have been verified in [9, 39, 40]. In the implementation,  $A_0^{-1}$  and the inverse for  $\frac{1}{\nu}I$  should be realized by applying a Multigrid algorithm or domain decomposition methods. Particularly, when Krylov subspace methods are used, these inverses should be applied inexactly (for example, using one V-cycle Multigrid algorithm to provide approximate inverses).

Let us denote

$$P_\pm = \begin{pmatrix} A_0 & 0 \\ 0 & \pm \frac{1}{\nu}I_h \end{pmatrix}, \quad (23)$$

We also propose another preconditioner of the block triangular type:

$$P_{T_1} = \begin{pmatrix} A_0 & 0 \\ B & -\frac{1}{\nu}I_h \end{pmatrix}, \quad (24)$$

by retaining the divergence operator. This preconditioner is still decoupled as the computation can be carried out in a block forward substitution manner. As an illustration, we illustrate the importance of using preconditioners in **Table 1**.

We use  $**$  to indicate that the iteration does not converge within the prescribed maximum number of iterations.  $N(P)$  refers to the number of iterations with a preconditioner  $P$ , and no preconditioner is applied when  $P$  is simply  $I$ . From the table, it is clear that both  $P_-$  and  $P_{T_1}$  accelerate the convergence of the GMRES method. The number of iterations based on the two preconditioners is independent of the mesh refinement. More numerical experiments for testing the robustness with respect to the physical parameters can be found in [9, 39].

### 2.3 Decoupling and linearization by two-level and multi-level algorithms

For the mixed Stokes/Darcy model, Mu and Xu in [11] propose a two-grid method in which the coarse grid solution is used to supplement the boundary conditions at the

$h$	DOF	$N(I)$	$N(P_-)$	$N(P_{T_1})$
$2^{-2}$	268	186	41	20
$2^{-3}$	948	432	45	22
$2^{-4}$	3556	* *	48	22
$2^{-5}$	13,764	* *	46	22
$2^{-6}$	54,148	* *	46	22

**Table 1.**  
 Number of iterations for the GMRES method without and with the two preconditioners  $P_-$  and  $P_{T_1}$ .

interface for both of the two subproblems. The **Two-grid Algorithm** proposed in [11] is composed by the following two steps.

1. Solve the linear part of problem  $(2.7)_H$  on a coarse grid: find  $\underline{u}_H = (\underline{u}_H, \phi_H) \in \underline{X}_H \subset \underline{X}_h, p_H \in Q_H \subset Q_h$  such that

$$\begin{cases} a(\underline{u}_H, \underline{v}_H) + b(\underline{v}_H, p_H) = (f, \underline{v}_H), & \forall \underline{v}_H = (\underline{v}_H, \psi_H) \in \underline{X}_H, \\ b(\underline{u}_H, q_H) = 0, & \forall q_H \in Q_H; \end{cases} \tag{25}$$

2. Solve a modified fine grid problem: find  $\underline{u}^H = (\underline{u}^h, \phi^h) \in \underline{X}_h, p^h \in Q_h$  such that

$$\begin{cases} a(\underline{u}^H, v_h) + b(v_h, p^h) = (f, v_h) - a_\Gamma(\underline{u}_H, v_h), & \forall v_h \in \underline{X}_h, \\ b(\underline{u}^H, q_h) = 0, & \forall q_h \in Q_h. \end{cases} \tag{26}$$

The main theoretical results for the two grid algorithm are as follows.

**Theorem 1.** *Let  $(\underline{u}_h, p_h)$  be the solution of coupled Stokes/Darcy model, and  $(\underline{u}^H, p^h)$  be defined by and (27) on the fine grid. The following error estimates hold:*

$$\|\phi_h - \phi^h\|_{H_p} \lesssim H^2, \tag{27}$$

$$\|\underline{u}_h - \underline{u}^h\|_{H_f} \lesssim H^{3/2}, \tag{28}$$

$$\|p_h - p^h\|_Q \lesssim H^{3/2}. \tag{29}$$

Based on this algorithm, some other improvements have been made. For example, in [18–20], by sequentially solving the Stokes submodel and the Darcy submodel, the authors can make  $\|\phi_h - \phi^h\|_{H_p}$ ,  $\|\underline{u}_h - \underline{u}^h\|_{H_f}$ , and  $\|p_h - p^h\|_Q$  are all of order  $H^2$ . Furthermore, Hou constructed a new auxiliary problem [16] for the Darcy submodel, and proved that Mu and Xu’s two-grid algorithm can retain  $\|\underline{u}_h - \underline{u}^h\|_{H_f}$  and  $\|p_h - p^h\|_Q$  order of  $H^2$ . It is remarkable that Mu and Xu’s two-grid algorithm is naturally parallel and of optimal order, if  $h$  is of order  $H^2$ .

The extension to a multilevel decoupled algorithm can be found in [26]. The **Multilevel Algorithm** is as follows:

1. Solve the linear part of problem  $(2.7)_H$  on a coarse grid: find  $\underline{u}_H = (\underline{u}_H, \phi_H) \in \underline{X}_H \subset \underline{X}_h, p_H \in Q_H \subset Q_h$  such that

$$\begin{cases} a(\underline{u}_H, \underline{v}_H) + b(\underline{v}_H, p_H) = f(\underline{v}_H), \forall \underline{v}_H = (\underline{v}_H, \psi_H) \in \underline{X}_H, \\ b(\underline{u}_H, q_H) = 0, \forall q_H \in Q_H; \end{cases} \quad (30)$$

2. Set  $h_0 = H$ , for  $j = 1$  to  $L$ ,

find  $u^{h_j} = (\underline{u}^{h_j}, \phi^{h_j}) \in \underline{X}_{h_j}, p^{h_j} \in Q_{h_j}$  such that

$$\begin{cases} a(u^{h_j}, v_{h_j}) + b(v_{h_j}, p^{h_j}) = f(v_{h_j}) - a_\Gamma(u^{h_{j-1}}, v_{h_j}), \quad \forall v_{h_j} \in \underline{X}_{h_j}, \\ b(u^{h_j}, q_{h_j}) = 0, \quad \forall q_{h_j} \in Q_{h_j}. \end{cases} \quad (31)$$

end.

In our multilevel algorithm, we refine the grid step by step, the coupled problem is only solved on the coarsest mesh, and linear decoupled subproblems are solved in parallel on successively refined meshes. We see that the algorithm is very effective and efficient. Moreover, the theory of the two grid algorithm guarantees that the approximation properties are good. As an illustration of the effectiveness of the multilevel algorithm [41], we present numerical results in **Table 2**.

In the following, we use steady state NS/Darcy model to illustrate how to apply two-level and multilevel methods to decouple the coupled nonlinear PDE models. The algorithm combines the two-level algorithms and the Newton-type linearization [4, 36, 42]. Our **Newton Type Linearization Based Two-level Algorithm** consists of the following three steps [17, 43].

1. Solve the coupled problem (19) on a coarse grid triangulation with the meshsize  $H$ : Find  $\underline{u}_H = (\underline{u}_H, \phi_H) \in \underline{X}_H$  and  $p_H \in Q_H$  such that

$$\begin{cases} a(\underline{u}_H, \underline{v}_H) + c(\underline{u}_H, \underline{u}_H, \underline{v}_H) + b(\underline{v}_H, p_H) = f(\underline{v}_H), \quad \forall \underline{v}_H = (\underline{v}_H, \psi_H) \in \underline{X}_H, \\ b(\underline{u}_H, q_H) = 0, \quad \forall q_H \in Q_H. \end{cases} \quad (32)$$

2. On a fine grid triangulation with the meshsize  $h \leq H$ , sequentially solve two decoupled and linearized local subproblems:

$h$	$ \phi^h - \phi _1$	$ \underline{u}^h - \underline{u} _1$	$ \underline{v}^h - \underline{v} _1$	$\ \underline{p}^h - \underline{p}\ _0$
$2^{-1}$	$4.592 \times 10^{-2}$	$1.550 \times 10^{-1}$	$1.066 \times 10^{-1}$	$8.410 \times 10^{-2}$
$2^{-2}$	$1.152 \times 10^{-2}$	$3.958 \times 10^{-2}$	$2.664 \times 10^{-2}$	$1.752 \times 10^{-2}$
$2^{-4}$	$7.280 \times 10^{-4}$	$2.466 \times 10^{-3}$	$1.652 \times 10^{-3}$	$1.040 \times 10^{-3}$
$2^{-8}$	$5.296 \times 10^{-6}$	$9.981 \times 10^{-6}$	$7.922 \times 10^{-6}$	$1.694 \times 10^{-5}$

**Table 2.**  
Errors between the solutions of multilevel algorithm and the exact solutions (second order discretization).

**Step a.** Solve a discrete Darcy problem in  $\Omega_p$ : Find  $\phi_h^* \in X_{p,h}$  such that

$$a_p(\phi_h^*, \psi_h) = \rho g(f_p, \psi_h)_{\Omega_p} + \rho g(\mathbf{u}_H \cdot \mathbf{n}_f, \psi_h)_\Gamma \quad \forall \psi_h \in X_{p,h}. \quad (33)$$

**Step b.** Solve a modified Navier–Stokes model using the Newton type linearization: Find  $\mathbf{u}_h^* \in \mathbf{X}_{f,h}$  and  $p_h^* \in Q_h$  such that

$$\begin{cases} a_f(\mathbf{u}_h^*, \mathbf{v}_h) + c(\mathbf{u}_H, \mathbf{u}_h^*, \mathbf{v}_h) + c(\mathbf{u}_h^*, \mathbf{u}_H, \mathbf{v}_h) + b(\mathbf{v}_h, p_h^*) = (f_f, \mathbf{v}_h)_{\Omega_f} \\ -\rho g(\phi_h^*, \mathbf{v}_h \cdot \mathbf{n}_f)_\Gamma + c(\mathbf{u}_H, \mathbf{u}_h^*, \mathbf{v}_h) + c(\mathbf{u}_h^*, \mathbf{u}_H, \mathbf{v}_h) \quad \forall \mathbf{v}_h \in \mathbf{X}_{f,h}, \\ b(\mathbf{u}_h^*, q_h) = 0 \quad \forall q_h \in Q_h. \end{cases} \quad (34)$$

3. On the same fine grid triangulation, solve two subproblems by using the newly obtained solution.

**Step a.** Solve a discrete Darcy problem in  $\Omega_p$ : Find  $\phi^h \in X_{p,h}$  such that

$$a_p(\phi^h, \psi_h) = \rho g(f_p, \psi_h)_{\Omega_p} + \rho g(\mathbf{u}_h^* \cdot \mathbf{n}_f, \psi_h)_\Gamma \quad \forall \psi_h \in X_{p,h}. \quad (35)$$

**Step b.** Correct the solution of the fluid flow model: Find  $\mathbf{u}^h \in \mathbf{X}_{f,h}$  and  $p^h \in Q_h$  such that

$$\begin{cases} a_f(\mathbf{u}^h, \mathbf{v}_h) + c(\mathbf{u}_H, \mathbf{u}^h, \mathbf{v}_h) + c(\mathbf{u}^h, \mathbf{u}_H, \mathbf{v}_h) + b(\mathbf{v}_h, p^h) = (f_f, \mathbf{v}_h)_{\Omega_f} \\ -\rho g(\phi^h, \mathbf{v}_h \cdot \mathbf{n}_f)_\Gamma + c(\mathbf{u}_H, \mathbf{u}_h^*, \mathbf{v}_h) + c(\mathbf{u}_h^*, \mathbf{u}_H - \mathbf{u}_h^*, \mathbf{v}_h) \quad \forall \mathbf{v}_h \in \mathbf{X}_{f,h}, \\ b(\mathbf{u}^h, q_h) = 0 \quad \forall q_h \in Q_h. \end{cases} \quad (36)$$

We remark here that the problem (36) and the problem (34) differ only in the right hand side. Similarly, the problem (35) and the problem (33) have the same stiffness matrix. In sum, the advantages of our work exist in that the scaling between the two meshsizes is better, the algorithm is decoupled and linear on the fine grid level and the two submodels in the last two steps share the same stiffness matrices.

For the coupled problem (19), by using the properties (16)–(18), the error estimates in the energy norm can be derived by using a fixed-point framework [4, 31]. Moreover, the Aubin-Nitsche duality argument can result in the  $L^2$  error analysis of the problem (19). In summary, we have.

**Lemma 1.** Let  $(\mathbf{u}, \phi, p) \in H^{k+1}(\Omega_f) \times H^{k+1}(\Omega_p) \times H^k(\Omega_f)$  be the solution of the Navier–Stokes/Darcy model (13) and  $(\mathbf{u}_h, \phi_h, p_h)$  be the FE solution of (19). We assume that  $\nu$  is sufficiently large and  $h$  is sufficiently small. There holds the following energy norm estimate for the problem (19).

$$|\mathbf{u} - \mathbf{u}_h|_{1,\Omega_f} + |\phi - \phi_h|_{1,\Omega_p} + \|p - p_h\|_{0,\Omega_f} \lesssim h^k. \quad (37)$$

Moreover, we have the following  $L^2$  error estimate:

$$\|\mathbf{u} - \mathbf{u}_h\|_{0,\Omega_f} + \|\phi - \phi_h\|_{0,\Omega_p} \lesssim h^{k+1}. \quad (38)$$

The energy norm estimate (37) is the Lemma 2 in [4]. The  $L^2$  error estimate (38) corresponds to the Lemma 3 in [4]. Detailed proofs of these results can be found in [4].

The following lemma concludes the error estimate of  $(\phi_h^*, \mathbf{u}_h^*, p_h^*)$  in the energy norm.

**Lemma 2. (Error analysis of the intermediate step two-level solution)** *Let  $(\phi, \mathbf{u}, p)$  and  $(\phi_h^*, \mathbf{u}_h^*, p_h^*)$  be defined by the problems (13) and (33)–(34), respectively. Under the assumptions of Lemma 1, there holds*

$$|\phi - \phi_h^*|_{1, \Omega_p} \lesssim H^{k+1} + h^k, \quad (39)$$

$$|\mathbf{u} - \mathbf{u}_h^*|_{1, \Omega_f} + \|p - p_h^*\|_{0, \Omega_f} \lesssim H^{k+1} + h^k. \quad (40)$$

$$\|\mathbf{u} - \mathbf{u}_h^*\|_{0, \Omega_f} \lesssim H^{2k+1} + H^{k+1}h + h^{k+1}. \quad (41)$$

From Lemma 1, we note that the optimal finite element solution error in the energy norm is of order  $O(h^k)$ . Combining the conclusions of this Lemma, we see that the intermediate step two-level solution error is still optimal in the energy norm if the scaling between the two meshsizes is taken to be  $h = H^{\frac{k+1}{k}}$ . The  $L^2$  error analysis is extended from [4, 20, 31, 37]. Let  $\mathbf{u}$  and  $\phi$  be the nonsingular solution of (13). From Lemma 1, the optimal  $L^2$  error for the finite element solution is of order  $O(h^{k+1})$ . To make sure  $\|\mathbf{u} - \mathbf{u}_h^*\|_{0, \Omega_f}$  is also of order  $O(h^{k+1})$ , the scaling between the two grids has to be taken as  $h = \max \left\{ H^{\frac{k+1}{k}}, H^{\frac{2k+1}{k+1}} \right\}$ . For instance, if  $k = 1$ , we have to set  $h = H^{\frac{3}{2}}$  to make sure the  $L^2$  error of  $\mathbf{u}_h^*$  is optimal. We now show that the final step two-level solution is indeed a good approximation to the solution of problem (13).

**Theorem 2. (Error analysis of the final step two-level solution)** *Let  $(\phi, \mathbf{u}, p)$  and  $(\phi^h, \mathbf{u}^h, p^h)$  be the solutions of (13) and (35)–(36) respectively. Under the assumptions of Lemma 1, the following error estimates hold:*

$$|\phi - \phi^h|_{1, \Omega_p} + |\mathbf{u} - \mathbf{u}^h|_{1, \Omega_f} + \|p - p^h\|_{0, \Omega_f} \lesssim H^{2k+1} + H^{k+1}h + h^k, \quad (42)$$

**Proposition 1.** *Let  $(\phi, \mathbf{u}, p)$  and  $(\phi^h, \mathbf{u}^h, p^h)$  be the solutions of (13) and (35)–(36) respectively. If we take  $h = H^{\frac{2k+1}{k}}$  for  $k = 1, 2$  and  $h = H^{\frac{k+1}{k-1}}$  for  $k \geq 3$ , then there holds the following error estimate.*

$$|\phi - \phi^h|_{1, \Omega_p} + |\mathbf{u} - \mathbf{u}^h|_{1, \Omega_f} + \|p - p^h\|_{0, \Omega_f} \lesssim h^k. \quad (43)$$

Finally, we would like to make some comments on the mixed Stokes/Darcy model. We note that by dropping those trilinear terms (32), (34) and (36), our two-level algorithm can be naturally applied to the coupled Stokes/Darcy model. We note that the above algorithms can be naturally extended to multi-level algorithms by recursively calling the above two-level algorithms [17, 43]. The extension and the corresponding analysis can be found in [26, 43].

## 2.4 Decoupled algorithms by partitioned time schemes

The fully evolutionary Stokes/Darcy equations will be used as the model problem in this subsection to illustrate the partitioned time schemes. We neglect

the fluid density and the porosity effects in this subsection. We review some decoupled methods that converge within a reasonable amount of time, and are stable when the physical parameters are small. More precisely, partitioned time methods can efficiently solve the surface subproblem and the subsurface subproblem separately.

For the estimate of the stability, we assume that the solution of the Stokes/Darcy problem is long-time regular [44]:

$$\begin{aligned} \mathbf{u} &\in W^{2,\infty}(0, \infty; L^2(\Omega_f)) \cap W^{1,\infty}(0, \infty; H^2(\Omega_f)), \\ \phi &\in W^{2,\infty}(0, \infty; L^2(\Omega_p)) \cap W^{1,\infty}(0, \infty; H^2(\Omega_p)), \\ p &\in L^{2,\infty}(0, \infty; H^1(\Omega_f)). \end{aligned} \quad (44)$$

The simplest time scheme for the evolutionary coupled Stokes/Darcy model is the **Backward Euler Algorithm**, which reads as: Given  $(\mathbf{u}_h^n, p_h^n, \phi_h^n) \in \mathbf{X}_{f,h} \times Q_h \times X_{p,h}$ , find  $(\mathbf{u}_h^{n+1}, p_h^{n+1}, \phi_h^{n+1}) \in \mathbf{X}_{f,h} \times Q_h \times X_{p,h}$ , such that for all  $\mathbf{v}_h \in \mathbf{X}_{f,h}, q_h \in Q_h, \psi_h \in X_{p,h}$ ,

$$\begin{cases} \left( \frac{\mathbf{u}_h^{n+1} - \mathbf{u}_h^n}{\Delta t}, \mathbf{v}_h \right) + a_f(\mathbf{u}_h^{n+1}, \mathbf{v}_h) - (p_h^{n+1}, \nabla \cdot \mathbf{v}_h) + g(\mathbf{v}_h \cdot \mathbf{n}_f, \phi_h^{n+1})_\Gamma = (f_f^{n+1}, \psi_h), \\ (q_h, \nabla \cdot \mathbf{u}_h^{n+1}) = 0, \end{cases} \quad (45)$$

$$gS_0 \left( \frac{\phi_h^{n+1} - \phi_h^{n-1}}{\Delta t}, \mathbf{v}_h \right) + a_p(\phi_h^{n+1}, \psi_h) - g(\mathbf{u}_h^{n+1} \cdot \mathbf{n}_f, \psi_h)_\Gamma = g(f_p^{n+1}, \psi_h). \quad (46)$$

However, this scheme is fully coupled and each time step one has to solve a coupled system including both (45) and (46), although, on the other hand, this scheme enjoys the desirable strong stability and convergence properties. In [12], Mu and Zhu propose the following backward Euler forward Euler scheme and combine it with the two-level spatial discretization. We neglect the two-level spatial discretization in this presentation. Here, the Forward Euler means it discretizes the coupling term explicitly. **Backward Euler Forward Euler Scheme (BEFE)**: given  $(\mathbf{u}_h^n, p_h^n, \phi_h^n) \in \mathbf{X}_{f,h} \times Q_h \times X_{p,h}$ , find  $(\mathbf{u}_h^{n+1}, p_h^{n+1}, \phi_h^{n+1}) \in \mathbf{X}_{f,h} \times Q_h \times X_{p,h}$ , such that for all  $\mathbf{v}_h \in \mathbf{X}_{f,h}, q_h \in Q_h, \psi_h \in X_{p,h}$ ,

$$\begin{cases} \left( \frac{\mathbf{u}_h^{n+1} - \mathbf{u}_h^n}{\Delta t}, \mathbf{v}_h \right) + a_f(\mathbf{u}_h^{n+1}, \mathbf{v}_h) - (p_h^{n+1}, \nabla \cdot \mathbf{v}_h) + g(\mathbf{v}_h \cdot \mathbf{n}_f, \phi_h^n)_\Gamma = (f_f^{n+1}, \psi_h), \\ (q_h, \nabla \cdot \mathbf{u}_h^{n+1}) = 0, \end{cases} \quad (47)$$

$$gS_0 \left( \frac{\phi_h^{n+1} - \phi_h^n}{\Delta t}, \mathbf{v}_h \right) + a_p(\phi_h^{n+1}, \psi_h) - g(\mathbf{u}_h^n \cdot \mathbf{n}_f, \psi_h)_\Gamma = g(f_p^{n+1}, \psi_h). \quad (48)$$

The analysis of this can be found in [12, 45]. In particular, the longtime stability (cf. (51)) of BEFE method was proved in [45] in the sense that no form of Gronwall's inequality was used.

**Theorem 3.** Assume the following time step condition is satisfied

$$\Delta t \lesssim \min \{ \nu k_{\min}^2, S_0 \nu^2 k_{\min} \}, \quad (49)$$

Then, BELF algorithm achieves the optimal convergence rate uniformly in time. The solution of the BEFE method satisfies the uniform in time error estimates:

i. If  $f_f \in L^\infty(0, +\infty; L^2(\Omega_f))$ ,  $f_p \in L^\infty(0, +\infty; L^2(\Omega_p))$ , then

$$\|u_h^n\|^2 + \|\phi_h^n\|^2 \leq C, \quad \forall n \geq 0. \quad (50)$$

ii. If  $\|f_f\|_{L^\infty(0, +\infty; L^2(\Omega_f))}$ ,  $\|f_p\|_{L^\infty(0, +\infty; L^2(\Omega_p))}$  are uniformly bounded in  $\Delta t$ , then

$$\|u_h^n\|^2 + \|\phi_h^n\|^2 + \Delta t \sum_{l=0}^n (\|\nabla u_h^l\|^2 + \|\nabla \phi_h^l\|^2) \leq C, \quad \forall n \geq 0. \quad (51)$$

The advantage of this scheme is that it is parallel. As revealed in the time step restriction (50), the disadvantage of this method is that it may become highly unstable when the parameters  $S_0$  and  $k_{min}$  are small. Another way for uncoupling surface/subsurface flow models is using splitting schemes which require sequential sub-problem solves at each time step [46]. As an example, we note that in solving (49), one can replace  $u_h^n$  by using the most updated solution obtained in the Stokes step. This will lead to Backward Euler time-split scheme [46]. We skip the details of this time-split method, interested readers can refer to [46]. By this way, one can design different sequential splitting schemes. Noting that the BEFE method is only of first order, in some other decoupled Implicit-explicit (IMEX) methods, one can combine of the three level implicit method with the coupling terms treated by the explicit method to achieve high order. For example, Crank–Nicolson Leap-Frog method [47, 48], second-order backward-differentiation with Gear's extrapolation, Adam-Moulton-Bashforth [49]. We present one of them: the **Crank–Nicolson Leap-Frog Method** for the evolutionary Stokes/Darcy model: given  $(u_h^{n-1}, p_h^{n-1}, \phi_h^{n-1})$ ,  $(u_h^n, p_h^n, \phi_h^n) \in \mathbf{X}_{f,h} \times Q_h \times X_{p,h}$ , find  $(u_h^{n+1}, p_h^{n+1}, \phi_h^{n+1}) \in \mathbf{X}_{f,h} \times Q_h \times X_{p,h}$ , such that for all  $v_h \in \mathbf{X}_{f,h}$ ,  $q_h \in Q_h$ ,  $\psi_h \in X_{p,h}$ ,

$$\begin{cases} \left( \frac{u_h^{n+1} - u_h^{n-1}}{2\Delta t}, v_h \right) + \left( \nabla \cdot \left( \frac{u_h^{n+1} - u_h^{n-1}}{2\Delta t}, v_h \right), \nabla \cdot v_h \right) + a_f \left( \frac{u_h^{n+1} + u_h^{n-1}}{2}, v_h \right) \\ - \left( \frac{p_h^{n+1} - p_h^{n-1}}{2}, \nabla \cdot v_h \right) + g(v_h, \phi_h^n)_\Gamma = (f_f^n, v_h), \\ \left( q_h, \nabla \cdot \frac{u_h^{n+1} - u_h^{n-1}}{2} \right) = 0, \end{cases} \quad (52)$$

$$gS_0 \left( \frac{\phi_h^{n+1} - \phi_h^{n-1}}{2\Delta t}, \phi_h \right) + a_p \left( \frac{\phi_h^{n+1} + \phi_h^{n-1}}{2}, \psi_h \right) - g(u_h^n, \psi_h)_\Gamma = g(f_p^n, \psi_h). \quad (53)$$

The Crank–Nicolson-Leap-Frog possesses strong stability and convergence properties [47, 48]. Most importantly, the time-step condition for the scheme does not depend on  $\kappa_{min}$ .

For the numerical experiments of these partitioned time schemes, we refer the readers to [12].

### 3. FSI models and decoupled algorithms

FSI models include a fluid model whose general form is (1), a structure model, plus certain interface conditions that describe the interaction mechanism (see **Figure 2** for an illustration of FSI models in the reference configuration and the deformed configuration). To differentiate the notations in different subdomains, we will use a subscript “*f*” to denote the variables in the fluid domain, and a subscript “*s*” to denote the variables in the structure domain.

In general, the structure model reads as:

$$\begin{cases} \rho_s \left( \frac{\partial \mathbf{u}_s}{\partial t} + (\mathbf{u}_s \cdot \nabla) \mathbf{u}_s \right) - \operatorname{div} \mathbf{T}(\mathbf{u}_s, p_s) = \mathbf{f}_s, & \forall \mathbf{x} \in \Omega_s, \\ \operatorname{div} \mathbf{u}_s = 0, & \forall \mathbf{x} \in \Omega_s. \end{cases} \quad (54)$$

Here,  $\rho_s$  is the density of the structure,  $\mathbf{u}_s$  is the structure velocity,  $p_s$  is the structure pressure. In structure mechanics, the displacement  $\mathbf{d}$  is usually used as a primary variable ( $\dot{\mathbf{d}} = \mathbf{u}_s$ ), and the stress term in the linear case can be described by using Hooke’s law. As the structure model is usually based on Lagrangian coordinates, researchers usually introduce the so-called Arbitrary Lagrangian Eulerian description for FSI models. In some special cases of FSI models, one can apply the simplified structure model such as 1D structure model or linear elasticity model for structure part, and the simplified fluid model such as linear Stokes or inviscid flow model for fluid part.

The fluid motion and the structure motion are coupled through certain interface conditions that describe the compatibility of the kinematics and transactions at the fluid–structure interface. For applications with non-slip interface conditions, both velocity and normal stress are continuous across the interface  $\Gamma$ , which may be described as

$$\begin{cases} \mathbf{u}_f = \mathbf{u}_s, & \text{on } \Gamma, \\ \mathbf{T}(\mathbf{u}_f, p_f) \mathbf{n} = \mathbf{T}(\mathbf{u}_s, p_s) \mathbf{n}, & \text{on } \Gamma. \end{cases} \quad (55)$$

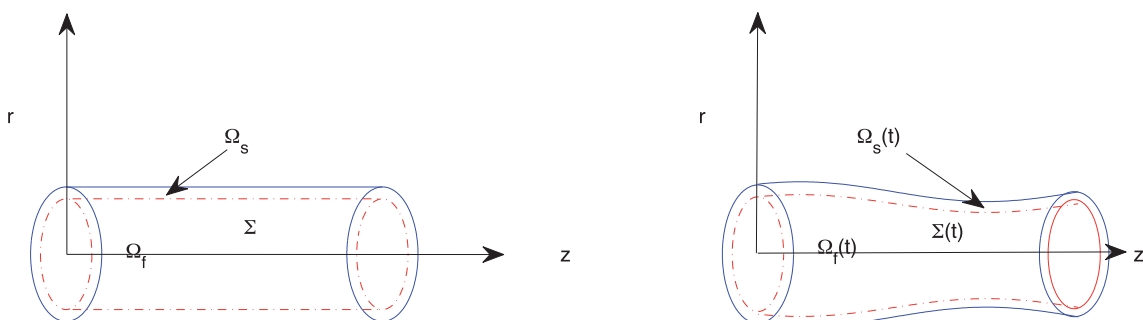


**Figure 2.**  
 An illustration of fluid structure interaction: the reference configuration (left) and the deformed configuration (right).

Here,  $\mathbf{n}$  denotes one of  $\mathbf{n}_f$  and  $\mathbf{n}_s$ . With suitable initial conditions and boundary conditions such as fluid flux boundary condition and structure Dirichlet boundary condition, the FSI models are complete.

There have been many advanced numerical methods for various FSI models. Our focus here is a linear fluid model coupled with a thin wall structure. The reason we choose this model is that this kind of models, if calculated using the standard (Dirichlet-Neumann) explicit decoupling schemes will lead to the so-called added mass effect [50]. Moreover, the algorithms dealing with the added-mass difficulties are the most exciting development in this direction. Therefore, we consider dropping the nonlinear term in (1), and consider the following 1D structure model:

$$\begin{cases} \rho_s \varepsilon \partial_t \dot{\mathbf{d}} + L_s(\mathbf{d}, \dot{\mathbf{d}}) = -T(\mathbf{u}_f, p_f) \mathbf{n}, & \text{on } \Gamma, \\ \mathbf{u}_s = \dot{\mathbf{d}} & \text{on } \Gamma. \end{cases} \quad (56)$$

Here,  $\varepsilon$  denotes the structure thickness,  $L_s(\mathbf{d}, \dot{\mathbf{d}})$  denotes the operator in the structure model, which may include both the elastic term and the damping term [14, 15].

### 3.1 Partitioned algorithms for FSI models

First of all, we comment here that the decoupled preconditioning techniques can also be naturally applied to FSI models. In the preconditioning step, one can apply either the Multigrid approach [51] or domain decomposition methods [52].

In this presentation, we focus on the two most recent approaches for the linear Stokes model coupled with thin wall structure. The first approach is called partitioned Robin-Neumann scheme, in which the fluid subproblem is imposed with Robin boundary condition at the interface while the structure subproblem is imposed with Neumann boundary conditioner at the interface [14, 15]. The second approach is called kinetically coupled  $\beta$ -scheme, which is actually decoupled in the sense that computations are realized subdomain by subdomain [13, 21]. The derivation of the  $\beta$ -scheme is based on operator splitting.

Partitioned Robin-Neumann scheme:

1. Given the initial solution  $\mathbf{u}_f^0, p_f^0$  and  $\mathbf{d}^0$ .

2. For  $m = 0, 1, 2, 3, \dots, N - 1$ ,

- **Fluid step:** find  $\mathbf{u}_f^{m+1}$  and  $p_f^{m+1}$  such that

$$\begin{cases} \frac{\rho_f}{\Delta t} (\mathbf{u}_f^{m+1} - \mathbf{u}_f^m) - \operatorname{div} T(\mathbf{u}_f^{m+1}, p_f^{m+1}) = \mathbf{0} & \text{in } \Omega_f, \\ \operatorname{div} \mathbf{u}_f^{m+1} = 0 & \text{in } \Omega_f, \\ T(\mathbf{u}_f^{m+1}, p_f^{m+1}) \mathbf{n} + \frac{\rho_s \varepsilon}{\Delta t} \mathbf{u}_f^{m+1} = \frac{\rho_s \varepsilon}{\Delta t} \dot{\mathbf{d}}^m + T(\mathbf{u}_f^m, p_f^m) \mathbf{n} & \text{on } \Gamma. \end{cases} \quad (57)$$

- **Structure step:** find  $\mathbf{d}_s^{m+1}$  such that

$$\begin{cases} \frac{\rho_s \varepsilon}{\Delta t} (\dot{\mathbf{d}}^{m+1} - \dot{\mathbf{d}}^m) + \mathbf{L}_s(\mathbf{d}^{m+1}, \dot{\mathbf{d}}^{m+1}) = -\mathbf{T}(\mathbf{u}_f^{m+1}, p_f^{m+1}) \mathbf{n} & \text{on } \Gamma, \\ \dot{\mathbf{d}}^{m+1} = \frac{1}{\Delta t} (\mathbf{d}^{m+1} - \mathbf{d}^m) & \text{on } \Gamma, . \end{cases} \quad (58)$$

3. End

Here,  $\frac{\rho_s \varepsilon}{\Delta t}$  is treated as a Robin coefficient. These partitioned iterative methods were firstly introduced in [53], as added-mass free alternatives to the standard Dirichlet-Neumann scheme. Some extensions and generalizations can be found in [14, 15].

Different from the partitioned Robin-Neumann scheme. The kinematically coupled  $\beta$ -scheme for the time-discrete problem is given as follows. The stability and the convergence rate of this scheme are analyzed in [13, 21].

1. Given the initial solution  $\mathbf{u}_f^0, p_f^0$  and  $\mathbf{d}^0$ .

2. For  $m = 0, 1, 2, 3, \dots, N - 1$ ,

- **Structure step:** find  $\tilde{\mathbf{u}}_s^{m+1}$  such that

$$\begin{cases} \rho_s \varepsilon \frac{\tilde{\mathbf{u}}_s^{m+1} - \mathbf{u}_s^m}{\Delta t} + \mathbf{L}_s(\mathbf{d}^{m+1}, \dot{\mathbf{d}}^{m+1}) = -\beta \sigma_f(\mathbf{u}_f^m, p_f^m) \mathbf{n} & \text{on } \Gamma, \\ \dot{\mathbf{d}}^{m+1} = \tilde{\mathbf{u}}_s^{m+1}, \mathbf{d}^{m+1} = \mathbf{d}^m + \Delta t \tilde{\mathbf{u}}_s^{m+1} & \text{on } \Gamma. \end{cases} \quad (59)$$

- **Fluid step:** find  $\mathbf{u}_f^{m+1}, p_f^{m+1}$  and  $\mathbf{u}_s^{m+1}$  such that

$$\begin{cases} \frac{\rho_f}{\Delta t} (\mathbf{u}_f^{m+1} - \mathbf{u}_f^m) - \text{div } \sigma_f(\mathbf{u}_f^{m+1}, p_f^{m+1}) = \mathbf{0} & \text{in } \Omega_f, \\ \text{div } \mathbf{u}_f^{m+1} = 0 & \text{in } \Omega_f, \\ \rho_s \varepsilon \frac{\mathbf{u}_s^{m+1} - \tilde{\mathbf{u}}_s^{m+1}}{\Delta t} = -\sigma_f(\mathbf{u}_f^{m+1}, p_f^{m+1}) \mathbf{n} + \beta \sigma_f(\mathbf{u}_f^m, p_f^m) \mathbf{n} & \text{on } \Gamma, \\ \mathbf{u}_f^{m+1} = \mathbf{u}_s^{m+1} & \text{on } \Gamma. \end{cases} \quad (60)$$

3. End.

### 3.2 Multirate time step approach for FSI models

Due to different time scales in many FSI problems, it is natural and essential to develop multirate time-stepping schemes [22, 23] that mimic the physical phenomena. For illustration, we will examine the application of the multirate technique to the  $\beta$ -scheme, since similar performance is observed for both the Robin-Neumann scheme and the  $\beta$ -scheme in numerical experiments. Furthermore, the decoupled multirate  $\beta$ -scheme can be extended to more general FSI problems involving nonlinearity, irregular domains, and large structural deformations.

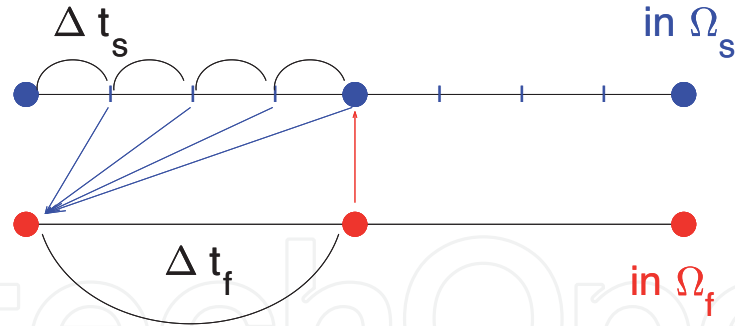


**Figure 3.**  
An illustration of a multirate time stepping technique.

In order to apply multirate time-stepping scheme to FSI problems, a question is in which region the larger time step size should be used. Numerical experiments suggest that the version with a larger time step size in the fluid solver (cf. **Figure 3**) results in a better accuracy. The corresponding method is described in the following. We comment here that the multirate  $\beta$ -scheme is nothing else but the  $\beta$ -scheme itself when the time-step ratio  $r = 1$ .

Multirate time-stepping  $\beta$ -scheme:

1. Given the initial solution  $\mathbf{u}_f^0, p_f^0$  and  $\mathbf{d}^0$ .

2. For  $k = 0, 1, 2, 3, \dots, N - 1$ , set  $m_k = r \cdot k$ .

• **Structure steps:** for  $m = m_k, m_k + 1, m_k + 2, \dots, m_{k+1} - 1$ ,

$$\begin{cases} \rho_s \varepsilon \frac{\tilde{\mathbf{u}}_s^{m+1} - \mathbf{u}_s^m}{\Delta t_s} + L_s(\mathbf{d}^{m+1}, \dot{\mathbf{d}}^{m+1}) = -\beta \sigma_f(\mathbf{u}_f^{m_k}, p_f^{m_k}) \mathbf{n} & \text{on } \Gamma, \\ \dot{\mathbf{d}}^{m+1} = \tilde{\mathbf{u}}_s^{m+1}, \mathbf{d}^{m+1} = \mathbf{d}^m + \Delta t_s \tilde{\mathbf{u}}_s^{m+1} & \text{on } \Gamma. \end{cases} \quad (61)$$

• **Fluid step:**

$$\begin{cases} \frac{\rho_f}{\Delta t_f} (\mathbf{u}_f^{m_{k+1}} - \mathbf{u}_f^{m_k}) - \operatorname{div} \sigma_f(\mathbf{u}_f^{m_{k+1}}, p_f^{m_{k+1}}) = \mathbf{0} & \text{in } \Omega_f, \\ \operatorname{div} \mathbf{u}_f^{m_{k+1}} = 0 & \text{in } \Omega_f, \\ \rho_s \varepsilon \frac{\mathbf{u}_s^{m_{k+1}} - \tilde{\mathbf{u}}_s^{m_{k+1}}}{\Delta t_f} = -\sigma_f(\mathbf{u}_f^{m_{k+1}}, p_f^{m_{k+1}}) \mathbf{n} + \beta \sigma_f(\mathbf{u}_f^{m_k}, p_f^{m_k}) \mathbf{n} & \text{on } \Gamma, \\ \mathbf{u}_f^{m_{k+1}} = \mathbf{u}_s^{m_{k+1}} & \text{on } \Gamma. \end{cases} \quad (62)$$

3. End.

### 3.3 Numerical experiment

In this subsection, we present numerical experiments to demonstrate the convergence and stability performance of the multirate  $\beta$ -scheme (60)–(61) for coupling a Stokes flow with a thin-walled structure by using a benchmark model. The model

consists of a 2-D rectangular fluid domain  $\Omega_f = [0, L] \times [0, R]$  with  $L = 6$  and  $R = 0.5$  and a 1-D structure domain  $\Gamma = [0, L] \times R$  that meanwhile also plays the role of the fluid–solid interface, as shown in **Figure 2**. The displacement of the interface is assumed to be infinitesimal and the Reynolds number in the fluid is assumed to be small (**Figure 4**). All the quantities will be given in terms of the centimeter-gram-second (CGS) system of units.

The physical parameters are set as follows:  $\rho_f = 1.0$ ,  $\rho_s = 1.1$ ,  $\mu = 0.035$ ;  
 $L_s(\mathbf{d}, \dot{\mathbf{d}}) = c_1 \partial_x^2 \mathbf{d} + c_0 \dot{\mathbf{d}}$ , where  $c_1 = \frac{E\varepsilon}{2(1+\nu)}$ ,  $c_0 = \frac{E\varepsilon}{R^2(1-\nu^2)}$  with  $\varepsilon = 0.1$ , the Poisson ratio  $\nu = 0.5$  and the Young's modulus  $E = 0.75 \cdot 10^6$ . A pressure-wave

$$P(t) = P_{max}(1 - \cos(2t\pi/T^*))/2 \quad \text{with} \quad P_{max} = 2 \cdot 10^4, \quad (63)$$

is prescribed on the fluid inlet boundary for  $T^* = 5 \cdot 10^{-3}$  (seconds). Zero traction is enforced on the fluid outlet boundary and no-slip condition is imposed on the lower boundary  $y = 0$ . For the solid, the two endpoints are fixed with  $\mathbf{d} = \mathbf{0}$  at  $x = 0$  and  $x = 6$ .

The first experiment is set up to compare the Robin-Neumann scheme with the  $\beta$ -scheme, the two stable decoupled methods recently developed for the benchmark model. **Figure 5** displays the displacements computed by the Robin-Neumann scheme and the  $\beta$ -scheme, together with the coupled implicit scheme for reference, where the

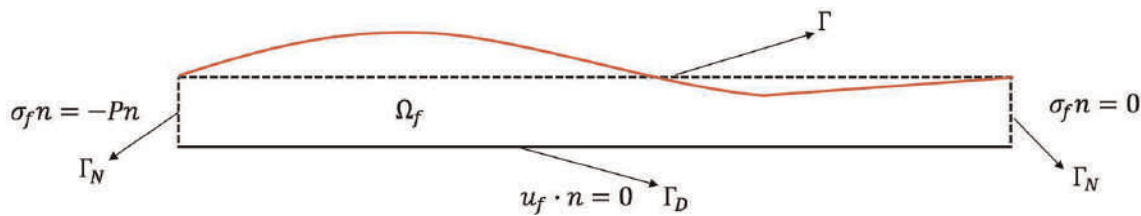


**Figure 4.**  
Geometrical configuration.

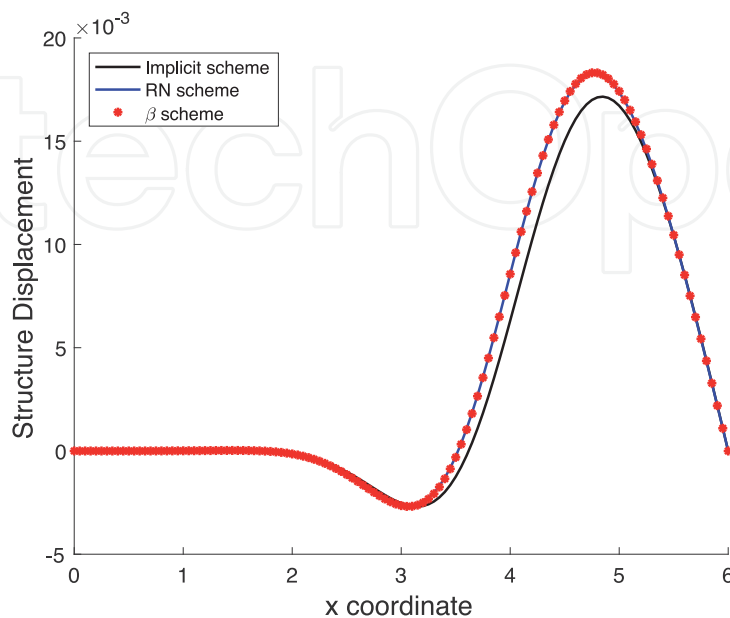


**Figure 5.**  
Comparisons of the numerical results obtained by the coupled implicit scheme, the RN scheme, and the  $\beta$ -scheme under the setting:  $h = 0.05$  and  $\Delta t_s = 10^{-4}$ .

mesh size and the time step size are  $h = 0.05$  and  $\Delta t = 10^{-4}$ . It is clearly seen that both decoupled schemes converge as well as the coupled implicit scheme. Moreover, little difference is observed between the two decoupled schemes numerically. This suggests we focus on the  $\beta$ -scheme for investigating the multirate time-step technique.

We then conduct numerical experiments to investigate the effects of the time-step ratio  $r$ . **Figure 6** illustrates that a larger time step size in the fluid part results in a more accurate numerical solution than that obtained by using a larger step size in the structure part. In the test, we fix  $h = 0.1$  and  $\Delta t = 10^{-5}$ . In addition, we observe that, when  $\frac{\Delta t_s}{\Delta t_f}$  is further increased to be  $\frac{\Delta t_s}{\Delta t_f} = 5$  or  $\frac{\Delta t_s}{\Delta t_f} = 10$ , there are substantial numerical instability. This screens out the possibility of using a larger time step size in the structure part.

To examine how the stability and approximation are affected when the time step in the fluid region is too large, we fix the time step  $\Delta t_s$  and  $h$  while varying the time-step ratio  $r = 1, 5, 10, 20, 50$ . **Figure 7** displays the computed displacements at  $t = 0.015$  with the structure time step size  $\Delta t_s = 10^{-5}$ , the mesh size  $h = 0.1$  (left) and  $h = 0.01$  (right). In the left figure, we observe that the structure displacements computed by using  $r = 1, 2, 5, 10$  approximate very well to that by using the coupled implicit scheme. To further investigate the stability and the convergence of the multirate  $\beta$ -scheme, in the right part of **Figure 7**, we reduce the mesh size to be  $h = 0.01$  while fixing the time step size. The numerical results confirm that the multirate  $\beta$ -scheme is still stable even the time-step ratio is reasonably large.

In **Figure 8**, we present the numerical results of the fluid pressure distribution at  $t = 0.005, 0.01, 0.015$ . From the top to the bottom, numerical results are: a reference solution by the coupled implicit scheme, the numerical solution by the  $\beta$ -scheme, and the solution by the multirate  $\beta$ -scheme with  $r = 10$ . By comparing the results, we see that the multirate  $\beta$ -scheme provides a very good approximation.

In order to examine the order of convergence, we start with  $h = 0.1$  and  $\Delta t_s = 0.0001$ , and then refine the mesh size by a factor of 2 and the time step size by a factor of 4. The space-time size settings are:

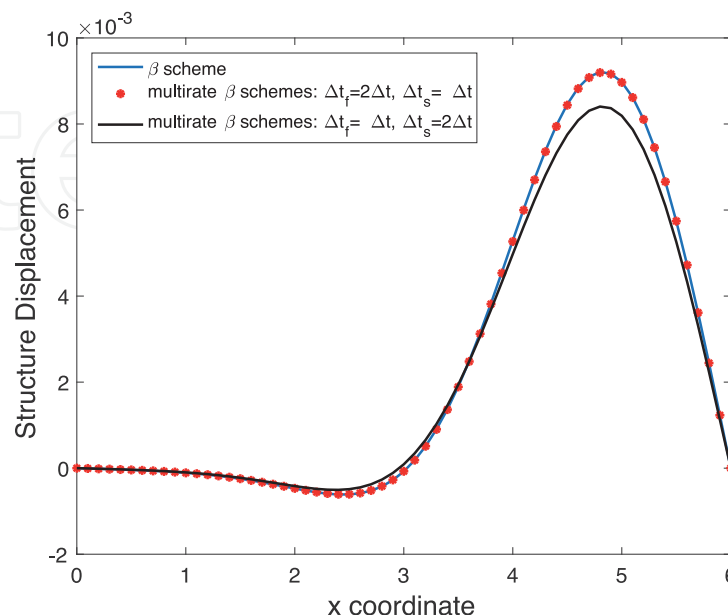


**Figure 6.** Comparison of the  $\beta$ -scheme and the multirate  $\beta$ -schemes with two different time-step ratios ( $h = 0.1$  and  $\Delta t = 10^{-5}$  are fixed).

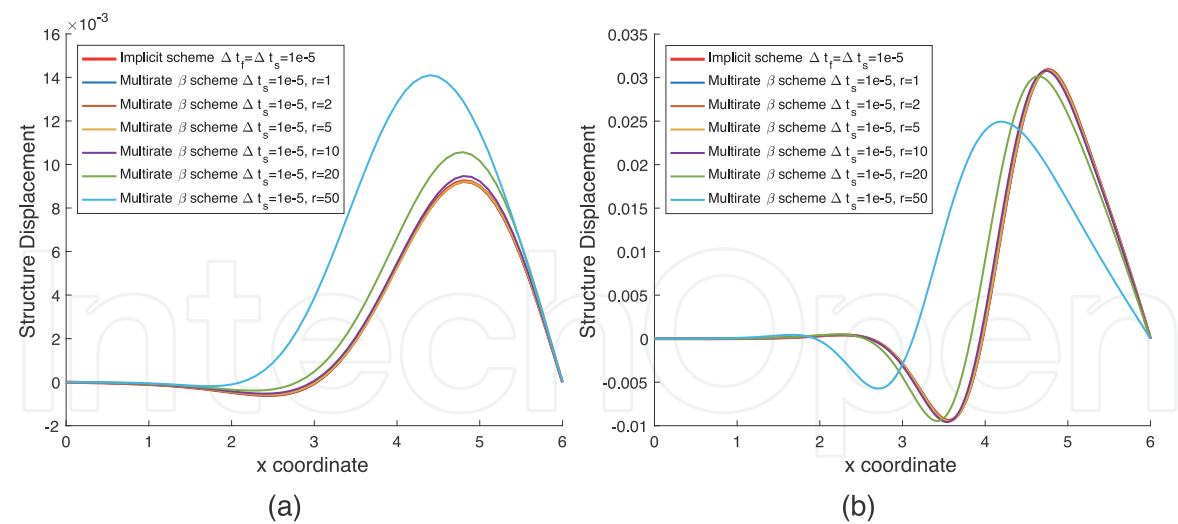


**Figure 7.**  
 Numerical displacements under the settings:  $h = 0.1$  (left)  $h = 0.01$  (right) and  $\Delta t_s = 10^{-5}$ .

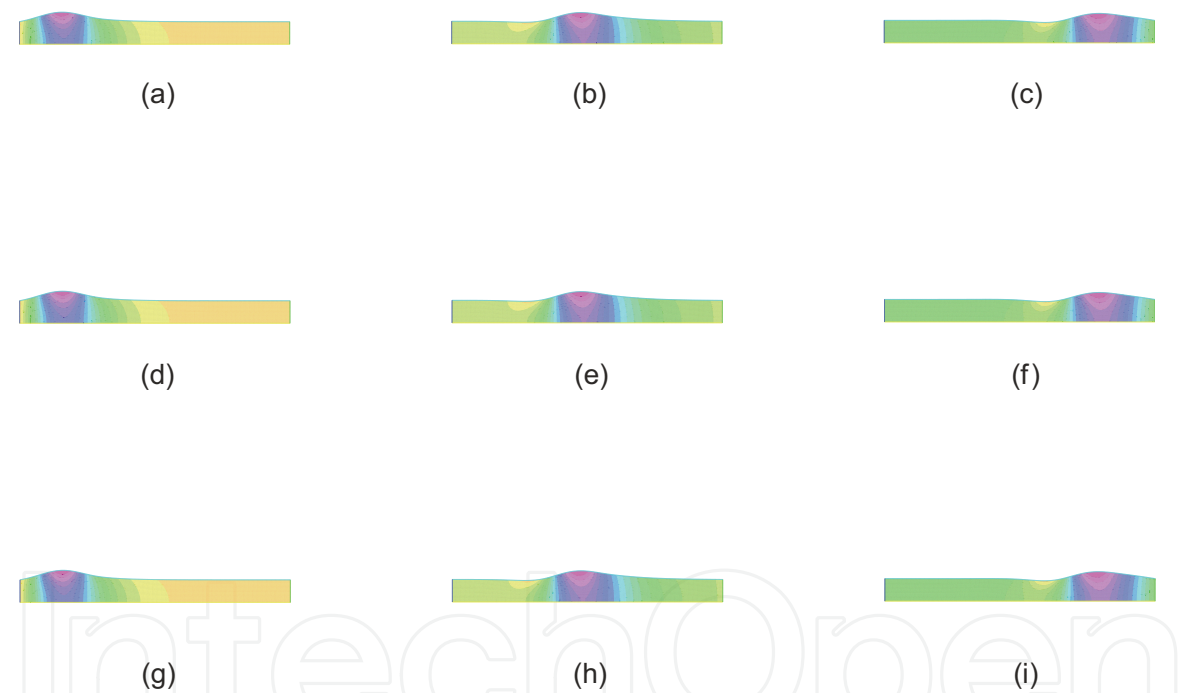


**Figure 8.**  
 Fluid pressure distribution at  $t = 0.005, 0.010, 0.015$  obtained by the coupled implicit scheme (top), the multirate  $\beta$ -scheme with  $r = 1$  (middle) and  $r = 10$  (bottom) with  $h = 0.01$  and  $\Delta t_s = 0.00001$ . (a)  $t = 0.005$ , (b)  $t = 0.010$ , (c)  $t = 0.015$ , (d)  $t = 0.005$ , (e)  $t = 0.010$ , (f)  $t = 0.015$ , (g)  $t = 0.005$ , (h)  $t = 0.010$ , (i)  $t = 0.015$ .

$$\{h, \Delta t_s\}^i = \left\{ 0.1 \cdot (0.5)^i, 0.0001 \cdot (0.25)^i \right\}, \quad i = 0, 1, 2, 3, 4. \tag{64}$$

We compare the numerical solutions of the multirate  $\beta$ -scheme with the reference solution. The reference solution is computed by using the coupled implicit scheme with a high space–time grid resolution ( $h = 3.125 \times 10^{-3}, \Delta t = 10^{-6}$ ) as that in [14]. In the multirate scheme,  $r = 1$  and  $r = 10$ . The relative errors of the primary variables ( $u_f, p_f$  and  $d$ ) at  $t = 0.015$  are displayed in **Figure 9**. From the comparisons, we see that the numerical errors are approximately reduced by a factor of 4 as the mesh size

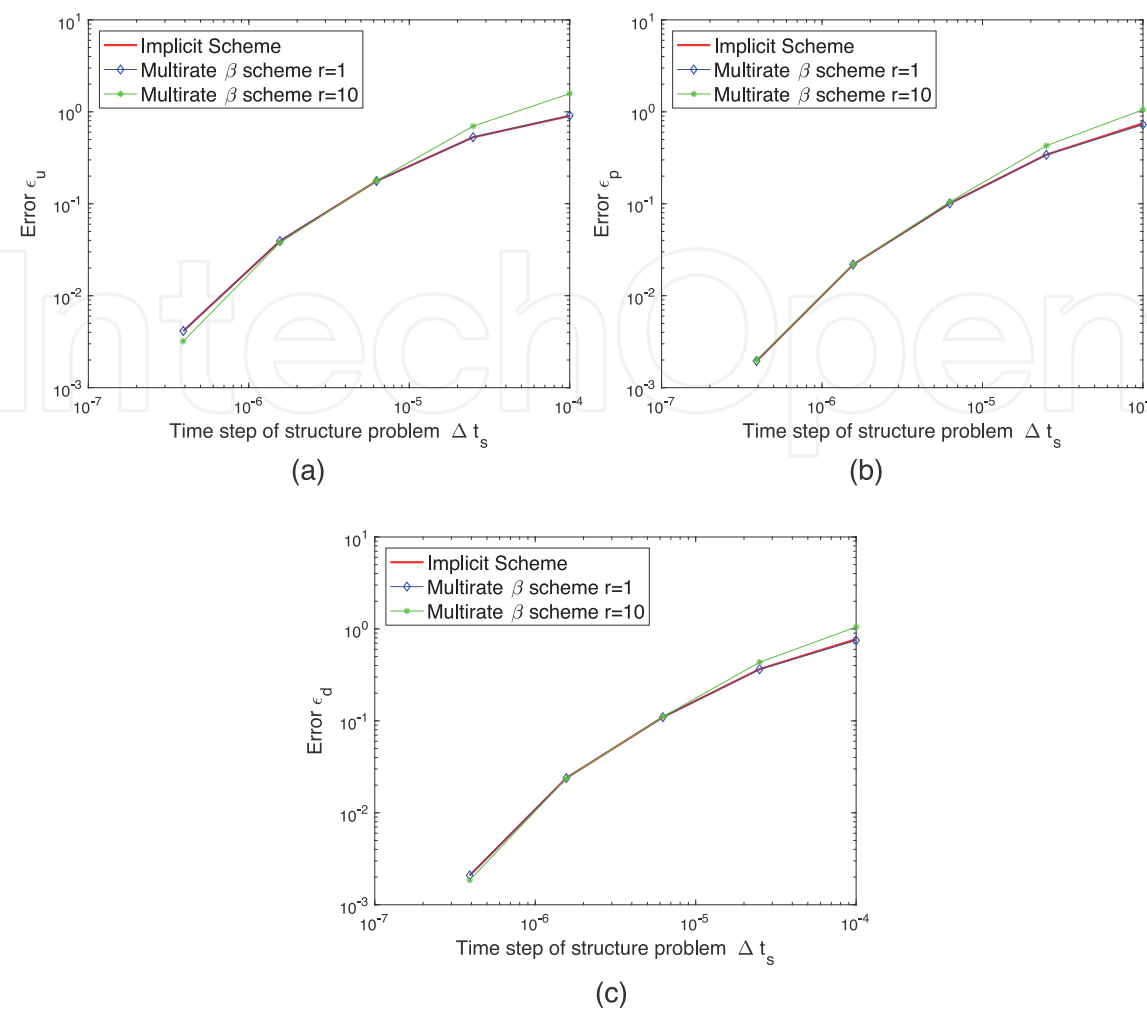


**Figure 9.** Relative errors of primary variables with the spacing  $h$  and time step size  $\Delta t_s$  in (64). (a) Relative error of  $u_f$ , (b) Relative error of  $p_f$ , (c) Relative error of  $d$ .

and the time step size are refined once. Therefore, the multirate  $\beta$ -scheme is of a second order in  $h$  and a first order in  $t$ .

Finally, in order to demonstrate the advantage of the multirate  $\beta$ -scheme, we compare in **Table 3** the CPU times of the concerned numerical algorithms under various settings. We fixed  $\Delta t_s = 10^{-5}$  and varying the mesh sizes as  $h = \frac{1}{10}, \frac{1}{20}, \frac{1}{40}, \frac{1}{80}, \frac{1}{160}$ . From the table, it is observed that the multirate  $\beta$ -scheme takes much less computational cost than that of the coupled implicit scheme, particularly when  $r$  is large.

	Implicit scheme	Multirate $\beta$ -scheme $r = 1$	Multirate $\beta$ -scheme $r = 10$
$h = \frac{1}{10}$	14.90	4.02	0.74
$h = \frac{1}{20}$	48.64	16.00	2.82
$h = \frac{1}{40}$	179.83	66.67	11.6
$h = \frac{1}{80}$	797.76	297.96	49.23
$h = \frac{1}{160}$	3165.26	1270.30	206.32

**Table 3.** CPU times (in seconds) for the coupled implicit scheme and the multirate  $\beta$ -scheme (with  $r = 1$  or  $10$ ) under different settings of mesh sizes ( $\Delta t_s = 10^{-5}$  is fixed).

#### **4. Concluding remarks**

In numerical methods for coupled multidomain PDE models, there are usually two types of methods: the monolithic methods and the partitioned (or decoupled) methods. The monolithic methods usually require a code developed for the coupled problem being solved globally. In contrast, the partitioned approach preserves software modularity because one can use existing subdomain solvers. The advantages of using monolithic methods exist in that they provide better approximation accuracy and usually have better stability than the decoupled methods. The drawback is that the computation costs based on the monolithic approaches are usually high. In comparison, the partitioned approaches allow reusing existing software which is an attractive advantage. However, the accuracy and stability of the partitioned method need to be taken into consideration. Nevertheless, from our research works, we also note that one can apply decoupling techniques in monolithic methods, for example, decoupled preconditioners and schemes which are parallel in time. On the other hand, in partitioned algorithms, one can also try to apply coupling numerical techniques such as extrapolations using previous time-step solutions, interpolation using the coarse-grid solution, or extrapolations between subdomain solutions. In this work, we review the decoupling algorithms for the coupled models of fluid flow interacting with porous media flow and FSI models. We show how to decouple the coupled PDE models using preconditioning, two-level and multi-level algorithms, and partitioned time schemes. We attach importance to the decoupling numerical techniques while also emphasizing how to preserve the coupled multidomain physics features. This review provides a general framework for designing decoupled algorithms for coupled PDE models and exhibits the philosophy of the interplays between PDE models and the corresponding numerical methods.

#### **Funding**

Mingchao Cai's work was supported in part by the NSF Awards (170023, 1831950), NIH-BUILD grant through UL1GM118973, NIH-RCMI grant through U54MD013376, and XSEDE HPC resource TG-MCH200022. Mo Mu's work was supported in part by the HongKong RGC CERG HKUST16301218.

IntechOpen

## Author details

Mingchao Cai<sup>1</sup>, Mo Mu<sup>2\*</sup> and Lian Zhang<sup>3</sup>

1 Department of Mathematics, Morgan State University, Baltimore, MD, USA


2 Department of Mathematics, The Hong Kong University of Science and Technology, Hong Kong

3 In-Chao Institute Ltd, Shenzhen, China

\*Address all correspondence to: [mamu@ust.hk](mailto:mamu@ust.hk)

## IntechOpen

---

© 2022 The Author(s). Licensee IntechOpen. This chapter is distributed under the terms of the Creative Commons Attribution License (<http://creativecommons.org/licenses/by/3.0>), which permits unrestricted use, distribution, and reproduction in any medium, provided the original work is properly cited. 

## References

- [1] Beavers G, Joseph D. Boundary conditions at a naturally permeable wall. *Journal of Fluid Mechanics*. 1967;**30**(1): 197-207
- [2] Saffman PG. On the boundary condition at the surface of a porous medium. *Studies in Applied Mathematics*. 1971;**50**(2):93-101
- [3] Jäger W, Mikelić A. On the interface boundary condition of Beavers, Joseph, and Saffman. *SIAM Journal on Applied Mathematics*. 2000;**60**:1111-1127
- [4] Cai M, Mu M, Xu J. Numerical solution to a mixed Navier-Stokes/Darcy model by the two-grid approach. *SIAM Journal on Numerical Analysis*. 2009;**47**(5):3325-3338
- [5] Cesmelioglu A, Girault V, Rivière B. Time-dependent coupling of Navier-Stokes and Darcy flows. *ESAIM: Mathematical Modelling and Numerical Analysis*. 2013;**47**:539-554
- [6] Girault V, Rivière B. DG approximation of coupled Navier-Stokes and Darcy equations by Beaver-Joseph-Saffman interface condition. *SIAM Journal on Numerical Analysis*. 2009;**47**: 2052-2089
- [7] Layton WJ, Schieweck F, Yotov I. Coupling fluid flow with porous media flow. *SIAM Journal on Numerical Analysis*. 2003;**40**(6):2195-2218
- [8] Layton W, Lenferink H. A multilevel mesh independence principle for the Navier-Stokes equations. *SIAM Journal on Numerical Analysis*. 1996;**33**(1):17-30
- [9] Cai M. Modeling and Numerical Simulation for the Coupling of Surface Flow with Subsurface Flow, [PhD thesis]. Hong Kong University of Science and Technology; 2008
- [10] Li Z. An augmented cartesian grid method for Stokes-Darcy fluid-structure interactions. *International Journal for Numerical Methods in Engineering*. 2016;**106**(7): 556-575
- [11] Mu M, Xu J. A two-grid method of a mixed stokes-Darcy model for coupling fluid flow with porous media flow. *SIAM Journal on Numerical Analysis*. 2007;**45**(5):1801-1813
- [12] Mu M, Zhu X. Decoupled schemes for a non-stationary mixed Stokes-Darcy model. *Mathematics of Computation*. 2010;**79**(270):707-731
- [13] Bukac M, Muha B. Stability and convergence analysis of the extensions of the kinematically coupled scheme for the fluid-structure interaction. *SIAM Journal on Numerical Analysis*. 2016;**54**(5): 3032-3061
- [14] Fernández M, Mullaert J, Vidrascu M. Explicit Robin-Neumann schemes for the coupling of incompressible fluids with thin-walled structures. *Computer Methods in Applied Mechanics and Engineering*. 2013;**267**:566-593
- [15] Fernández M, Mullaert J, Vidrascu M. Generalized Robin-Neumann explicit coupling schemes for incompressible fluid-structure interaction: Stability analysis and numerics. *International Journal for Numerical Methods in Engineering*. 2015;**101**(3):199-229
- [16] Hou Y. Optimal error estimates of a decoupled scheme based on two-grid finite element for mixed Stokes-Darcy model. *Applied Mathematics Letters*. 2016;**57**:90-96
- [17] Huang P, Cai M, Wang F. A Newton type linearization based two grid method

for coupling fluid flow with porous media flow. *Applied Numerical Mathematics*. 2016;**106**:182-198

[18] Zuo L, Hou Y. A decoupling two-grid algorithm for the mixed Stokes-Darcy model with the Beavers-Joseph interface condition. *Numerical Methods for Partial Differential Equations*. 2014;**30**(3):1066-1082

[19] Zuo L, Hou Y. Numerical analysis for the mixed Navier-Stokes and Darcy problem with the Beavers-Joseph interface condition. *Numerical Methods for Partial Differential Equations*. 2015;**31**(4):1009-1030

[20] Zhang T, Yuan J. Two novel decoupling algorithms for the steady Stokes-Darcy model based on two-grid discretizations. *Discrete and Continuous Dynamical Systems—Series B*. 2014;**19**(3):849-865

[21] Čanić S, Muha B, Bukač M. Stability of the kinematically coupled  $\beta$ -scheme for fluid-structure interaction problems in hemodynamics. *International Journal of Numerical Analysis and Modeling*. 2015;**12**(1):54-80

[22] Rybak I, Magiera J, Helmig R, Rohde C. Multirate time integration for coupled saturated/unsaturated porous medium and free flow systems. *Computational Geosciences*. 2015;**19**(2): 299-309

[23] Zhang L, Cai M, Mu M. A multirate approach for fluid-structure interaction computation with decoupled methods. *Communications in Computational Physics*. 2020;**27**(4):1014-1031

[24] Badia S, Codina R. Unified stabilized finite element formulations for the stokes and the Darcy problems. *SIAM Journal on Numerical Analysis*. 2009;**47**(3):1971-2000

[25] Burman E, Hansbo P. A unified stabilized method for Stokes' and Darcy's equations. *Journal of Computational and Applied Mathematics*. 2007;**198**(1): 35-51

[26] Cai M, Mu M. A multilevel decoupled method for a mixed Stokes/Darcy model. *Journal of Computational and Applied Mathematics*. 2012;**236**(9): 2452-2465

[27] Discacciati M, Miglio E, Quarteroni A. Mathematical and numerical models for coupling surface and groundwater flows. *Applied Numerical Mathematics*. 2002;**43**(1):57-74

[28] Discacciati M, Quarteroni A. Convergence analysis of a subdomain iterative method for the finite element approximation of the coupling of Stokes and Darcy equations. *Computing and Visualization in Science*. 2004;**6**(2-3): 93-103

[29] Discacciati M, Quarteroni A, Valli A. Robin-Robin domain decomposition methods for the Stokes-Darcy coupling. *SIAM Journal on Numerical Analysis*. 2007;**45**(3):1246-1268

[30] Rivière B, Yotov I. Locally conservative coupling of Stokes and Darcy flows. *SIAM Journal on Numerical Analysis*. 2005;**42**(5):1959-1977

[31] Girault V, Raviart PA. *Finite Element Methods for Navier-Stokes Equations, Theory and Algorithms*, Springer Series in Computational Mathematics. Vol. 5. Berlin: Springer; 1986

[32] Elman H, Silvester D, Wathen A. *Finite Elements and Fast Iterative Solvers: With Applications in Incompressible Fluid Dynamics*. Oxford University Press; 2014

- [33] Nield D, Bejan A. Convection in Porous Media. Vol. Vol. 3. Springer; 2006
- [34] Badea L, Discacciati M, Quarteroni A. Numerical analysis of the Navier-Stokes/Darcy coupling. *Numerische Mathematik*. 2010;**115**(2):195-227
- [35] Quarteroni A, Valli A. Domain Decomposition Methods for Partial Differential Equations. Oxford University Press; 1999
- [36] Layton W, Tobiska L. A two-level method with backtracking for the Navier-Stokes equations. *SIAM Journal on Numerical Analysis*. 1998;**35**(5):2035-2054
- [37] Brezzi F, Fortin M. Mixed and Hybrid Finite Element Methods. New York: Springer-Verlag; 1991
- [38] Taylor S, Hood P. A numerical solution of the Navier-Stokes equations using the finite element technique. *Computers & Fluids*. 1973;**1**:73-100
- [39] Cai M, Mu M, J. Xu preconditioning techniques for a mixed Stokes/Darcy model in porous media applications. *Journal of Computational and Applied Mathematics*. 2009;**233**(2):346-355
- [40] Kay D, Loghin D, Wathen A. A preconditioner for the steady-state Navier-Stokes equations. *SIAM Journal on Scientific Computing*. 2002;**24**(1): 237-256
- [41] Layton W, Lee H, Peterson J. Numerical solution of the stationary Navier-Stokes equations using a multilevel finite element method. *SIAM Journal on Scientific Computing*. 1998; **20**:1-12
- [42] Dai X, Cheng X. A two-grid method based on Newton iteration for the Navier-Stokes equations. *Journal of Computational and Applied Mathematics*. 2008;**220**(1):566-573
- [43] Cai M, Huang P, Mu M. Some multilevel decoupled algorithms for a mixed Navier-Stokes/darcy model. *Advances in Computational Mathematics*. 2017:1-31
- [44] Adams RA. Sobolev Spaces. New York: Academic Press; 1975
- [45] Layton W, Tran H, Trenchea C. Analysis of long time stability and errors of two partitioned methods for uncoupling evolutionary groundwater-surface water flows. *SIAM Journal on Numerical Analysis*. 2013;**51**(1):248-272
- [46] Layton W, Tran H, Xiong X. Long-time stability of four methods for splitting the evolutionary Stokes-Darcy problem into Stokes and Darcy sub-problems. *Journal of Computational and Applied Mathematics*. 2012;**236**:3198-3217
- [47] Kubacki M. Uncoupling evolutionary groundwater-surface water flows using the Crank-Nicolson Leap-Frog method. *Numerical Methods for Partial Differential Equations*. 2013;**29**: 1192-1216
- [48] Kubacki M, Moraiti M. Analysis of a second-order, unconditionally stable, partitioned method for the evolutionary Stokes-Darcy model. *International Journal of Numerical Analysis and Modeling*. 2015;**12**:704-730
- [49] Chen W, Gunzburger M, Sun D, Wang X. Efficient and long-time accurate second-order methods for Stokes-Darcy system. *SIAM Journal on Numerical Analysis*. 2013;**51**:2563-2584
- [50] Causin P, Gerbeau J, Nobile F. Added-mass effect in the design of

partitioned algorithms for fluid–structure problems. *Computer Methods in Applied Mechanics and Engineering*. 2005;**194**(42):4506–4527

[51] Xu J, Yang K. Well-posedness and robust preconditioners for discretized fluid–structure interaction systems. *Computer Methods in Applied Mechanics and Engineering*. 2015;**292**: 69–91

[52] Wu Y, Cai X. A fully implicit domain decomposition based ale framework for three-dimensional fluid–structure interaction with application in blood flow computation. *Journal of Computational Physics*. 2014;**258**: 524–537

[53] Badia S, Nobile F, Vergara C. Fluid–structure partitioned procedures based on Robin transmission conditions. *Journal of Computational Physics*. 2008; **227**:7027–7051